THE ASTRONOMICAL JOURNAL, 165:100 (28pp), 2023 March

https://doi.org/10.3847/1538-3881/acad84

Metal Mixing in the *r*-process Enhanced Ultrafaint Dwarf Galaxy Reticulum II[*]

Alexander P. Ji[1,2,3], Joshua D. Simon[4], Ian U. Roederer[3,5], Ekaterina Magg[6], Anna Frebel[3,7], Christian I. Johnson[8], Ralf S. Klessen[9,10], Mattis Magg[9,11], Gabriele Cescutti[12,13,14], Mario Mateo[5], Maria Bergemann[6,15], and John I. Bailey, III[16]

[1] Department of Astronomy & Astrophysics, University of Chicago, 5640 S Ellis Avenue, Chicago, IL 60637, USA; alexji@uchicago.edu
[2] Kavli Institute for Cosmological Physics, University of Chicago, Chicago, IL 60637, USA
[3] Joint Institute for Nuclear Astrophysics—Center for the Evolution of the Elements (JINA-CEE), USA
[4] Observatories of the Carnegie Institution for Science, 813 Santa Barbara Street, Pasadena, CA 91101, USA
[5] Department of Astronomy, University of Michigan, 1085 S. University Avenue, Ann Arbor, MI 48109, USA
[6] Max Planck Institute for Astronomy, Königstuhl 17, Heidelberg, D-69117, Germany
[7] Department of Physics & Kavli Institute for Astrophysics and Space Research, Massachusetts Institute of Technology, Cambridge, MA 02139, USA
[8] Space Telescope Science Institute, 3700 San Martin Drive, Baltimore, MD 21218, USA
[9] Universität Heidelberg, Zentrum für Astronomie, Institut für Theoretische Astrophysik, D-69120 Heidelberg, Germany
[10] Universität Heidelberg, Interdiszipliäres Zentrum für Wissenschaftliches Rechnen, D-69120 Heidelberg, Germany
[11] International Max Planck Research School for Astronomy and Cosmic Physics at the University of Heidelberg (IMPRS-HD), Germany
[12] Dipartimento di Fisica, Sezione di Astronomia, Università di Trieste, Via G.B. Tiepolo 11, I-34143 Trieste, Italy
[13] INAF, Osservatorio Astronomico di Trieste, Via Tiepolo 11, I-34143 Trieste, Italy
[14] INFN, Sezione di Trieste, Via A. Valerio 2, I-34127 Trieste, Italy
[15] Niels Bohr International Academy, Niels Bohr Institute, University of Copenhagen, Blegdamsvej 17, DK-2100 Copenhagen, Denmark
[16] Department of Physics, UCSB, Santa Barbara, CA 93016, USA

Abstract

The ultrafaint dwarf galaxy Reticulum II was enriched by a single rare and prolific *r*-process event. The *r*-process content of Reticulum II thus provides a unique opportunity to study metal mixing in a relic first galaxy. Using multi-object high-resolution spectroscopy with VLT/GIRAFFE and Magellan/M2FS, we identify 32 clear spectroscopic member stars and measure abundances of Mg, Ca, Fe, and Ba where possible. We find $72^{+10}_{-12}\%$ of the stars are *r*-process-enhanced, with a mean $\langle[\mathrm{Ba/H}]\rangle = -1.68 \pm 0.07$ and unresolved intrinsic dispersion $\sigma_{[\mathrm{Ba/H}]}<0.20$. The homogeneous *r*-process abundances imply that Ret II's metals are well mixed by the time the *r*-enhanced stars form, which simulations have shown requires at least 100 Myr of metal mixing in between bursts of star formation to homogenize. This is the first direct evidence of bursty star formation in an ultrafaint dwarf galaxy. The homogeneous dilution prefers a prompt and high-yield *r*-process site, such as collapsar disk winds or prompt neutron star mergers. We also find evidence from [Ba/H] and [Mg/Ca] that the *r*-enhanced stars in Ret II formed in the absence of substantial pristine gas accretion, perhaps indicating that ≈70% of Ret II stars formed after reionization.

Unified Astronomy Thesaurus concepts: Dwarf galaxies (416); Local Group (929); R-process (1324); Chemical abundances (224); Galaxy chemical evolution (580)

Supporting material: machine-readable table

1. Introduction

Ultrafaint dwarf galaxies (UFDs) are Milky Way satellite galaxies with luminosities $M_V > -7.7$ (stellar masses $\lesssim 10^5 M_\odot$, Simon 2019). UFDs appear to form all their stars in the first 1–2 billion years, before their star formation is cut off by reionization (Benson et al. 2002; Brown et al. 2014). UFDs probe the extreme low-mass end of galaxy formation, where star formation is inefficient and massive stars form stochastically, resulting in intermittent feedback and incomplete sampling of nucleosynthetic sources (Koch et al. 2008, 2013; Frebel et al. 2010; Simon et al. 2010; Frebel & Norris 2015; Ji et al. 2016a, 2019c). UFDs are also relics of early galaxy formation, providing a unique window into the

first stars and galaxies in a pre-reionization universe, as well as a clean probe of the first metal-free Population III stars (e.g., Bovill & Ricotti 2009; Salvadori & Ferrara 2009; Frebel & Bromm 2012; Ji et al. 2015). Because many halo stars with [Fe/H] < −2.5 likely form in UFD-like environments, even if they later grow into or accrete into larger systems (Brauer et al. 2019), it is crucial to understand the star formation conditions for UFDs to interpret the most metal-poor stars. To understand these early properties, the red giant branch stars in UFDs have been the subject of intense spectroscopic study. The last 15 yr have resulted in high-resolution spectra of $\gtrsim 100$ stars across ~20 UFDs with detailed elemental abundances (see Frebel & Norris 2015; Simon 2019; Ji et al. 2019c, 2020b for a description of the basic characteristics and chemical evolution trends).

Reticulum II (Ret II) is a UFD discovered in the Dark Energy Survey (Bechtol et al. 2015; Koposov et al. 2015a), located only 32 kpc away. Initial follow-up spectroscopy showed that its velocity dispersion, mean metallicity, and metallicity dispersion were consistent with typical UFDs (Simon et al. 2015; Koposov et al. 2015b; Walker et al. 2015;

henceforth S15; K15; W15). Subsequent high-resolution spectroscopy surprisingly showed that most Ret II stars displayed some of the highest *r*-process enhancements known (Ji et al. 2016a, 2016b; Roederer et al. 2016b, henceforth J16, R16). By comparing with other UFDs (which display unusually low neutron-capture element abundances, Frebel & Norris 2015; Ji et al. 2019c), the clear conclusion is that Ret II experienced enrichment from a single rare and prolific *r*-process event. The source of the *r*-process elements is still debated, as it could be consistent with *r*-process nucleosynthesis in a prompt neutron star merger or rare core-collapse supernova (e.g., Beniamini et al. 2016; Ji et al. 2016a; Safarzadeh & Scannapieco 2017; Ojima et al. 2018; Safarzadeh et al. 2019a; Siegel et al. 2019; Tarumi et al. 2020; Cowan et al. 2021; Jeon et al. 2021; Molero et al. 2021).

The single *r*-process event in Ret II provides a unique opportunity to probe *metal mixing* in a UFD. Because all the *r*-process elements (including barium and europium) were deposited in a single enrichment event, the distribution of *r*/H ratios in Ret II stars depends *only* on the overall amount of enriched gas and the homogeneity of metal mixing into the gas. This contrasts with elements synthesized by more common sources like supernovae or asymptotic giant branch (AGB) stars, because the frequency of element production interacts with metal mixing to produce the distribution of stellar abundances (e.g., Krumholz & Ting 2018; Emerick et al. 2019, 2020). A direct constraint on metal mixing by measuring the [*r*/H] distribution could play a major role in interpreting UFD abundances and formation histories (e.g., Frebel & Bromm 2012; Ji et al. 2015; Webster et al. 2016; Tarumi et al. 2020).

We thus present a detailed spectroscopic study of Ret II chemical abundances obtained with multi-object spectroscopy using Very Large Telescope (VLT)/FLAMES and Magellan/M2FS. We find 32 clear member stars and eight more candidates, the most spectroscopically confirmed members to date in Ret II. About half the stars have Ba and Fe constraints, while a third have Mg and/or Ca measurements as well. Our primary focus is measuring the distribution of [Ba/H] in these stars, which is a tracer of *r*-process enrichment in Ret II due to the high *r*-process enhancement and negligible *s*-process contribution in Ret II (Ji et al. 2016a). Because this is the largest spectroscopic sample of members yet, we also explore more general kinematics, binarity, chemical evolution, and spatial gradients. Section 2 presents the spectroscopic observations and data reduction. Section 3 describes the velocity and chemical abundance analysis methods, as well as membership determination, including auxiliary information from the Dark Energy Survey (DES, DES Collaboration et al. 2018) and Gaia EDR3 (Gaia Collaboration et al. 2016, 2021; Lindegren et al. 2021). Section 4 gives our results for the Ret II radial velocity distribution, chemical abundance trends, Fe and Ba distributions, and radial gradients. Section 5 discusses the implications of our measurements on metal mixing in dwarf galaxies, the origin of the *r*-process elements, and chemical evolution in Ret II. We summarize and conclude in Section 6. Multi-epoch velocities are provided in Appendix A. A major systematic for our Ba results is microturbulence, which is discussed extensively in Appendices B and C.

2. Observations and Data Reduction

We observed Reticulum II with VLT/FLAMES in 2017 October (Pasquini et al. 2002), and with Magellan/M2FS in 2016 September at medium resolution and 2017 November at high resolution (Mateo et al. 2012). Table 1 contains details about which stars were observed at which settings. Note that all signal-to-noise ratios (S/Ns) quoted in this paper refer to the S/N per pixel.

2.1. VLT/FLAMES, GIRAFFE

The FLAMES/GIRAFFE setup on the VLT UT2 provides high-resolution spectra of ~100 stars over a field of view of diameter 0°.4. Observations were taken in visitor mode on 2017 October 26–27 with excellent weather. We used the HR14A setting, covering one order from 6300–6500 Å with $R \sim 18,000$. Targets were selected based on our own photometry of public DES Y1 images following Koposov et al. (2015a). We chose targets near the fiducial color–magnitude diagram (CMD) within the single field we targeted. The total FLAMES exposure time was 11.8 hr, with most exposures being 3000 s but a few exposures of 2400 s and 3600 s at the end of the night.

Data were reduced with the standard ESO pipeline, which provides flat-corrected and wavelength calibrated 1D flux and error spectra. The 1D spectra are extracted to a common rebinned dispersion without cosmic ray rejection or sky subtraction. For each object, we removed cosmic rays in 1D by normalizing individual exposures by their median flux, then masking pixels with $>5\sigma$ deviations from the combined median spectrum. Care was taken not to mask pixels associated with variable sky lines. Sky subtraction was performed in 1D mostly following Battaglia et al. (2008). For each exposure, we constructed a master sky spectrum from ~15 sky fibers using an inverse-variance weighted mean. The master sky flux was split into two components, a sky emission line and a continuum component. The line component was used to identify wavelength bins associated with emission lines. Then for each object spectrum, we also split the flux into emission lines and continuum, rescaled the master sky line flux to match the object emission line flux by minimizing the L1 norm (total absolute deviation at wavelengths associated with sky emission lines), applied the same scaling factor to the sky continuum, and subtracted the rescaled master sky from the object spectrum. Visual inspection of the sky-subtracted spectra suggests this procedure was generally effective, with no correction to the line-spread function or wavelength recalibration needed. Still, there are sometimes sky subtraction residuals from spatially variable sky lines, which does affect our Ba line of interest (see Section 2.4). Final coadded spectra were obtained using an inverse-variance weighted average of individual exposures.

2.2. Magellan/M2FS HiRes

We obtained high-resolution spectra of Ret II stars with M2FS on 2017 November 16–17. We used the HiRes mode with 180 μm slits, providing $R \sim 18,000$. The detectors were binned 2×2 with four amplifier slow readout. Two different blocking filters were used to observe the targets (one on each M2FS channel), based on a visual examination of the VLT spectra. For fainter targets with unclear Ba detections or upper limits, we used the `BulgeGC1` filter, which includes 24 fibers covering six orders from 6100 to 6700 Å, including the Ba line

Table 1
Observations

ID	R.A. (h:m:s)	Decl. (d:m:s)	g_0 (mag)	r_0 (mag)	r_e/r_h	v_{hel} (km s^{-1})	σ_v (km s^{-1})	$\mu_\alpha \cos\delta$ (mas yr^{-1})	μ_δ (mas yr^{-1})	Mem	Bin	S/N px^{-1} (VLT)	HiRes Mode	S/N px^{-1} (HiRes)	S/N px^{-1} (MedRes)
1	03:35:23.8	−54:04:07.66	16.45	15.65	0.60	+65.3	0.2	2.43	−1.39	M	N	140	⋯	⋯	94
2	03:36:07.7	−54:02:35.58	17.43	16.81	0.57	+62.5	3.0	2.39	−1.33	M	Y	73	MgWide	39	58
3	03:34:47.9	−54:05:25.03	17.49	16.87	1.49	+62.0	0.4	2.36	−1.39	M	N	94	MgWide	34	57
4	03:35:31.1	−54:01:48.24	17.61	17.02	0.79	+58.5	0.3	2.25	−1.35	M	N	69	MgWide	37	68
5	03:35:48.0	−54:03:49.84	18.27	17.69	0.39	+61.7	0.3	2.28	−1.29	M	N	76	MgWide	19	40
6	03:35:37.1	−54:04:01.25	18.57	18.03	0.37	+64.3	0.4	2.50	−1.60	M	N	65	MgWide	24	25
7	03:35:56.3	−54:03:16.29	18.86	18.38	0.39	+63.2	0.4	2.28	−1.34	M	N	50	MgWide	14	26
8	03:34:57.6	−54:05:31.42	18.94	18.40	1.25	+60.2	0.4	2.34	−1.28	M	N	52	MgWide	15	29
9	03:34:54.2	−54:05:58.05	18.93	18.42	1.35	+69.2	0.4	2.40	−1.36	M	N	52	MgWide	17	33
10	03:35:21.0	−54:03:48.16	18.93	18.43	0.68	+64.5	4.6	2.24	−1.20	M	Y	53	MgWide	15	⋯
11	03:35:02.5	−54:03:54.27	19.23	18.73	1.20	+67.0	0.9	2.68	−1.40	M	N	⋯	BulgeGC1	12	30
12	03:35:58.1	−54:02:04.78	19.30	18.81	0.27	+64.6	0.5	2.35	−1.13	M	N	39	MgWide	15	29
13	03:35:11.7	−54:03:21.81	19.31	18.83	1.00	+67.0	3.4	2.71	−1.31	M	Y	42	MgWide	10	⋯
14	03:34:39.7	−54:07:54.37	19.37	18.84	1.82	+62.3	0.7	2.54	−1.51	C	N	40	BulgeGC1	10	⋯
15	03:36:01.8	−54:04:05.49	19.57	19.07	0.81	+62.6	0.6	2.18	−1.21	M	N	34	BulgeGC1	12	⋯
16	03:35:50.1	−54:01:39.24	19.72	19.29	0.39	+64.6	0.9	2.47	−1.63	C	N	30	MgWide	10	⋯
17	03:35:13.7	−54:04:56.72	19.67	19.20	0.87	+60.2	0.7	2.52	−1.30	M	N	32	BulgeGC1	12	27
18	03:35:17.0	−54:04:03.05	19.68	19.20	0.77	+65.5	8.0	2.52	−1.08	M	Y	21	BulgeGC1	12	⋯
19	03:35:15.2	−54:08:43.03	19.69	19.21	1.81	+67.8	11.1	2.39	−1.07	M	Y	31	BulgeGC1	12	22
20	03:35:14.0	−54:05:58.19	19.98	19.53	1.01	+63.6	0.7	2.76	−1.60	M	N	27	BulgeGC1	5	⋯
21	03:36:35.8	−54:01:20.21	20.19	19.73	1.23	+61.0	0.8	2.32	−1.37	M	N	16	BulgeGC1	7	⋯
22	03:36:21.9	−54:00:40.68	20.29	19.85	0.86	+65.6	0.7	2.02	−2.11	M	N	15	BulgeGC1	5	⋯
23	03:35:24.0	−54:02:26.69	20.28	19.85	0.82	+61.6	0.7	2.70	−1.78	M	N	19	BulgeGC1	6	⋯
24	03:35:02.9	−54:01:09.84	20.38	19.94	1.81	+63.6	0.8	3.11	−1.14	M	N	19	BulgeGC1	4	⋯
25	03:35:44.2	−54:01:50.03	20.41	19.93	0.43	+62.0	0.7	2.22	−2.30	M	N	20	BulgeGC1	6	⋯
26	03:35:35.4	−54:02:54.88	20.72	20.38	0.36	+61.5	0.8	2.83	−1.63	M	N	13	BulgeGC1	4	⋯
97	03:36:27.7	−53:58:26.31	17.13	16.27	1.34	+67.5	0.7	2.34	−1.29	C	N	125	⋯	⋯	⋯
99	03:35:14.5	−54:02:33.16	20.39	19.92	1.08	+67.2	0.8	2.50	−0.90	M	N	19	BulgeGC1	7	⋯
100	03:36:18.7	−53:57:45.14	18.04	18.20	1.53	+61.0	0.8	2.46	−1.48	M	N	⋯	MgWide	25	⋯
102	03:36:12.7	−53:56:02.25	18.05	18.23	2.16	+66.8	0.7	2.19	−1.21	M	N	⋯	MgWide	28	⋯
134	03:35:12.5	−54:00:59.16	20.82	20.47	1.58	+62.2	1.0	3.01	−1.90	M	N	13	MgWide	2	⋯
142	03:35:38.7	−54:04:55.59	20.89	20.42	0.67	+61.0	0.7	2.36	−1.46	C	N	14	MgWide	3	⋯
143	03:35:39.5	−54:00:23.48	20.93	20.62	1.07	+58.9	0.9	3.59	−2.82	C	N	10	MgWide	3	⋯
144	03:35:39.4	−54:03:57.31	20.93	20.67	0.35	+65.0	1.1	2.06	−1.47	M	N	11	MgWide	2	⋯
151	03:35:47.5	−54:03:25.05	20.59	20.36	0.23	+68.0	1.0	2.68	−0.51	C	N	14	⋯	⋯	⋯
154	03:36:05.4	−54:02:06.36	20.41	20.21	0.44	+61.9	1.0	2.70	−1.46	C	N	13	⋯	⋯	⋯
157	03:36:11.6	−54:00:34.45	20.64	20.23	0.71	+67.9	0.9	1.94	−2.10	M	N	12	BulgeGC1	5	⋯
188	03:34:59.3	−53:58:23.98	20.90	20.59	2.79	+68.4	1.2	2.05	−2.94	C	N	7	⋯	⋯	⋯
192	03:35:16.9	−54:05:22.59	20.69	20.29	0.87	+69.1	0.9	1.89	−1.77	M	N	17	BulgeGC1	4	⋯
195	03:35:16.5	−54:04:36.12	20.60	20.21	0.78	+68.1	0.8	2.14	−2.22	M	N	14	BulgeGC1	4	⋯

Note. Positions and photometry from DES. Half-light radius assuming Mutlu-Pakdil et al. (2018) structural parameters. Heliocentric radial velocities and uncertainties are the average systematics-corrected uncertainties described in Section 3.2 and Appendix A. Proper motions are from Gaia EDR3. The HiRes and MedRes columns refer to M2FS observations described in this paper. Only the member and candidate member stars are shown here. The full table is available in electronic form in the online journal.

(This table is available in its entirety in machine-readable form.)

at 6496.7 Å. The Ba line at 6141 Å is on the blue end of the filter cutoff and cannot be used. For brighter targets that already had clear Ba detections in the VLT data or upper limits, we instead used the `MgWide` filter, which includes 28 targets covering four orders from 5150 to 5400 Å. Six sky fibers were allocated for each arm. The total exposure time was 14h.

The data were reduced with a custom pipeline.[17] Each of four amplifier images was bias subtracted using the overscan and stitched into one image, then had dark current subtracted. Every science frame was associated with a single arc and flat obtained closest in time to the science frame. The object trace was fitted to each flat using a fifth-order Legendre polynomial. Scattered light was subtracted from every flat and science frame by fitting the inter-object regions with a 2D Legendre polynomial of degree 5 in either direction. Twilight flats were used to determine throughput corrections for each fiber.

The wavelength calibration was motivated by Kelson (2003) and adapted for fiber spectroscopy. An initial feature identification was done once by hand, extracting all orders of each fiber and using the IRAF `identify` command to manually identify positions of 50–70 arc lines in each order of each fiber in the X (wavelength) direction on the CCD (Tody 1986, 1993). These identifications were then turned back into 2D coordinates using the trace functions. The actual wavelength calibration was performed in 2D, finding sources in each arc frame using `Source Extractor` (Bertin & Arnouts 1996), and matching the detected sources to identified lines using a KD tree.[18] We then fit a fifth-order Legendre polynomial for the wavelength solution, iteratively rejecting outliers, and using lines from all object fibers to fit the overall distortion. A single X and Y pixel offset is allowed for each fiber (but not orders within a fiber) to account for any movement of the fibers in the pseudo-slit. In total, 40–50 lines were identified and used in each order for the `MgWide` filter, and 10–30 lines were identified and used for the `BulgeGC1` filter (fewer due to the saturated arcs). The final wavelength solution has a typical RMS < 0.01 Å in both arms. Data were then extracted using flat-relative optimal extraction (Zechmeister et al. 2014), which we found performed better than fitting a functional form to the object profile.

To perform sky subtraction, we linearly rebinned the extracted spectra onto a uniform wavelength grid, then followed essentially the same sky subtraction procedure as for the VLT data. The main differences were that the M2FS data have multiple orders, so sky subtraction was done independently for each order, and because the `MgWide` filter has few sky lines, we did not rescale the master sky spectrum to match line strengths, instead just directly subtracting the throughput-corrected master sky. There were clear differences in the line-spread function for different fibers, resulting in residuals around sky lines. We thus rejected data around sky lines. Different exposures were coadded order-by-order with an inverse-variance weighted average. Coadded orders were then continuum-normalized separately in `smhr`[19] before being stitched into a single spectrum.

2.3. Magellan/M2FS MedRes

We conducted two sets of medium-resolution observations of Ret II stars using M2FS on 2016 September 6 and 10, totaling 6.72 hr of integration time. We used the MedRes grating on the "R" spectrograph, 95 μm slits, 2×2 binning, and the `MedRes_Ba(23)` filter, which transmits one order with $4450 \leqslant \lambda \leqslant 4615$ Å. This setup yields $R \sim 9000$, as measured from individual Ar or Th emission lines in the comparison lamp spectra. We performed data reduction, extraction, wavelength calibration, sky subtraction, coaddition, and continuum normalization following the procedures described in Roederer et al. (2016a), modified for use with MedRes spectra.

We extracted the two sets of Ret II MedRes spectra (one set from each night) separately. We measured radial velocities of each star in each observation by cross-correlating (using the IRAF `fxcor` task) its spectrum against a synthetic metal-poor template spectrum smoothed to the same spectral resolution. Repeat observations of probable Ret II members show a standard deviation of 1.7 km s^{-1}, which we regard as the uncertainty of an individual measurement. We also observed two comparison stars, CD $-24°1782$ and CS 31082–001, using the same M2FS MedRes setup. Their radial velocities, after applying heliocentric corrections computed using the IRAF `rvcorrect` task, agree with published values (Roederer et al. 2014; Hansen et al. 2015) to better than 1.7 km s^{-1}, which we regard as the systematic uncertainty of our measurements. Combining the individual and systematic uncertainty, we adopt a total velocity uncertainty of 2.4 km s^{-1} for the MedRes velocities. However, when later comparing repeat velocity measurements of Ret II stars, we found a systematic offset of ≈ 10 km s^{-1}. We thus decided not to use the M2FS MedRes velocities in this work, though we report their values in Appendix A.

2.4. Comment on Sky Subtraction and Ba Lines

Our primary Ba line at 6496.7 Å is very close to a strong sky line at 6498.7 Å, and our Ba abundances are potentially susceptible to sky subtraction residuals. For the VLT data with $S/N > 25$, we were able to obtain good simultaneous fits to the Ba lines and the sky line residuals. We decided stars with $S/N < 25$ were too strongly affected by sky subtraction to have reliable Ba measurements, especially because a small error can make a big asymmetric difference in the abundances for saturated lines (Section 3.4.2). For the M2FS data, the signal-to-noise was lower and the heliocentric correction moved the Ba line right into the sky line, so none of the Ba 6496.7 Å line measurements from M2FS was reliable. There was also a 6141 Å Ba line located on the filter cutoff, but after investigation we decided it was adversely affected by scattered light subtraction systematics and thus not sufficiently reliable for abundance measurements.

3. Analysis

We assigned each star a numerical ID. IDs 1–26 were red giant branch stars identified as members or candidate members by Simon et al. (2015; a superset of Walker et al. 2015; Koposov et al. 2015b), sorted by magnitude. IDs 97–200 were assigned arbitrarily to other observed stars.

---

[17] https://github.com/alexji/m2fs_reduction

[18] 2D wavelength calibration was necessary for the `BulgeGC1` filter because the ThArNe arcs taken for this setting were extremely saturated, introducing many spurious features in 1D extracted arcs.

[19] https://github.com/andycasey/smhr, originally described in Casey (2014) and expanded in Ji et al. (2020a).
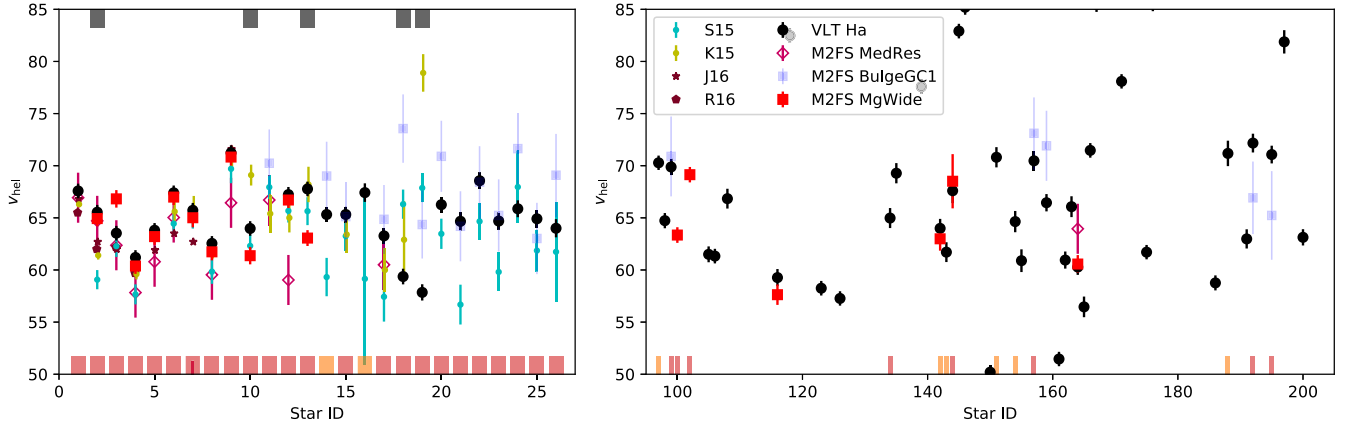
Figure 1. Individual radial velocity measurements for all stars from this study and the literature. No systematic velocity corrections have been applied in this figure. The left panel shows red giant branch stars *previously* marked as confirmed or candidate members, while the right panel shows other stars. Along the bottom axis, red bars indicate stars that are certain members, while orange lines indicate candidate members. Along the top axis, gray lines indicate binary stars.

3.1. Photometry and Astrometry

For all observed stars, we queried the DES DR1 catalog for *griz* magnitudes using NOAO data lab, which were dereddened using the DES DR1 reddening coefficients (DES Collaboration et al. 2018). The exception is star ID 1, which is saturated in the DES data release but had photometry determined from an individual DECam exposure in Simon et al. (2015). The subscript 0 (e.g., g_0) indicates dereddened magnitudes. R.A. and decl. were taken from the DES catalog (differing by $\sim 0\rlap{.}''1$ compared to Gaia). We also computed the elliptical distance r_e for each star, assuming Ret II is centered at 03:35:47.83 −54:02:47.8 with a position angle of 68°, an ellipticity of 0.6, and a half-light radius of 6.3 arcmin (Mutlu-Pakdil et al. 2018). We adopted a distance modulus of 17.5 whenever needed (Mutlu-Pakdil et al. 2018). Proper motions $\mu_\alpha \cos\delta$ and μ_δ were obtained by cross-matching with Gaia EDR3 (Lindegren et al. 2021). Our spectroscopic target selection did not use proper motions, as it was performed before Gaia DR2 was released.

3.2. Radial Velocities

Radial velocities were measured with weighted cross-correlation against a high-resolution template spectrum of HD 122563 obtained with the Magellan Inamori Kyocera Echelle spectrograph and shifted to rest frame (Bernstein et al. 2003). Each spectrum was first normalized with a third-order polynomial. Then, for a range of velocities, we shifted the template spectrum by that velocity and calculated the χ^2 of pixels within a specific wavelength interval. For the VLT data and the M2FS `BulgeGC1` data, we used Hα to measure velocities, cross-correlating from 6550–6575 Å. For the M2FS `MgWide` data, we used the Mg triplet, cross-correlating from 5150–5200 Å. Velocities were then found as the minimum of the χ^2 contour, and 1σ statistical velocity errors were determined by $\Delta\chi^2 = 1$ (e.g., Martini et al. 2006). For the M2FS data, we used just one of the orders for velocity measurement: order 54 for `BulgeGC1` and order 69 for `MgWide`. We did not attempt to determine very detailed radial velocities for the MedRes M2FS data, given its lower resolution.

We determined systematic velocity uncertainties from repeated velocity measurements. For both the VLT and M2FS run, every star was observed with 7–15 individual exposures over two nights. We thus measured the velocity and

statistical uncertainty for each individual exposure. Then, following Li et al. (2019), we took all pairs of repeated velocity measurements with $\sigma_v < 30$ km s^{-1} and fit the following Gaussian-plus-outlier model:

$$v_i - v_j \sim f\mathcal{N}(0, \sqrt{F(\sigma_{v,i})^2 + F(\sigma_{v,j})^2})$$
$$+ (1-f)\mathcal{N}(0, \sigma_{\text{outlier}}) \qquad (1)$$

where v_i, v_j, $\sigma_{v,i}$, and $\sigma_{v,j}$ are the individual velocities and uncertainties; f is the fraction of pairs that are good; σ_{outlier} is a large value characterizing a broad background outlier model; and $F(\sigma_v) = \sqrt{\sigma_{v,\text{floor}}^2 + (k \times \sigma_v)^2}$ is a rescaling of the velocity uncertainty with a scale factor k and a systematic floor $\sigma_{v,\text{floor}}$. The VLT data had $f = 0.98$, $\sigma_{v,\text{floor}} = 0.69$ km s^{-1}, and $k = 1.02$. The M2FS `MgWide` data had $f = 0.66$, $\sigma_{v,\text{floor}} = 0.74$ km s^{-1}, and $k = 1.64$. The M2FS `BulgeGC1` data had $f = 0.93$, $\sigma_{v,\text{floor}} = 3.20$ km s^{-1}, and $k = 0.11$. In this case, having $k < 1$ suggests that the individual velocities are dominated by systematic errors, which is primarily due to the low S/N of individual exposures causing poor continuum fits and template matches. We thus conservatively take $k = 1$ for the `BulgeGC1` data. These values of k and $\sigma_{v,\text{floor}}$ are applied to generate our final velocity uncertainties.

Figure 1 shows the individual velocity measurements for all observed stars. The left panel shows the 26 likely members from previous observations, while the right panel shows other observed stars. The red bars on the lower axis indicate stars that are clear members, while orange bars indicate candidate members (see Section 3.3 for the definitions). For comparison, in the left panel we also plot velocities derived by S15, K15, J16, and R16. Because many literature velocities were measured using the same spectra, duplicate velocity measurements from W15 and S15 were removed from this figure.

For the 40 members and candidate members (determined in Section 3.3), we determined velocities by averaging our VLT and M2FS velocities with the literature velocities from S15, K15, J16, and R16, for a total of up to six independent velocity measurements. We combine all available literature velocities with an inverse-variance weighted mean. Details are given in Appendix A, but this includes estimating a systematic velocity offset for each data sample using the S15 velocities as a reference, and identifying binary star candidates using a

chi-squared test. Five candidate binary stars are identified in Table 1 and as gray bars on the top axis of Figure 1. These binary star velocities were also found with a weighted mean, but the uncertainty indicates the range of velocities. Binary candidates are excluded from the velocity and velocity dispersion calculations. Our focus in this paper is on chemical abundances, so this assessment of binarity and velocity systematics is incomplete, and a more comprehensive future study is warranted.

3.3. Membership

We used four criteria to establish membership within our selected targets: radial velocities in the range $53\ \mathrm{km\,s^{-1}} < v_{\rm r,\ hel} < 74\ \mathrm{km\,s^{-1}}$; proper motion within two units of Mahalanobis distance from the Ret II mean proper motion of $(\mu_\alpha^*, \mu_\delta) = (2.39, -1.36)$ (McConnachie & Venn 2020);[20] position within two elliptical half-light radii of the Ret II center[21]; and $g_0 - r_0$ color between 13 Gyr, α-enhanced Dartmouth isochrones (Dotter et al. 2008) with [Fe/H] = −2.5 and [Fe/H] = −1.5, allowing a 0.03 mag buffer on each side of the isochrone given an expected reddening uncertainty. Because we used hard cuts, edge cases near these boundaries were inspected individually.

The results are shown in Figure 2. Seventy of the 129 total spectroscopic targets were rejected as being outside our radial velocity limits (small blue points). Of the remaining 59 stars, 18 stars had consistent radial velocities but were rejected based on clearly discrepant spatial location, CMD position, or proper motion (cyan crosses). One additional star (ID 191) was also rejected as having [Fe/H] ∼ −0.5 from our later analysis, too high to be part of Ret II. This leaves 40 stars, of which 32 stars were confident members, clearly matching at least three of the four criteria (large red points). In the rest of this paper, we refer to these stars as "clear members." The remaining eight stars were highlighted as uncertain members (small orange squares), which we refer to as "candidate members" in the rest of this paper. Stars 188 and 143 are CMD members but at somewhat large distance and proper motion away from the galaxy core to be considered very confident members. Stars 14, 97, and 142 are redward of the isochrones, requiring high metallicities [Fe/H] ≳ −1.5 (or perhaps large carbon bands) to be considered part of Ret II. Our subsequent analysis finds that none of these stars has such a high metallicity. Star 16 is blueward of the isochrone and has an unusually shallow Hα line shape, suggesting it is a hotter star. Finally, stars 151 and 154 have consistent kinematics and would be CMD nonmembers, but they are located where evolved blue stragglers or an unusually young stellar population might be found, as indicated by a 10 Gyr isochrone in the top-left panel of Figure 2. In other dwarf spheroidal galaxies, blue stragglers tend to appear even younger (2.5 ± 0.5 Gyr, Santana et al. 2013), so it is possible these stars could indicate a younger population of stars in Ret II. However, the spectra of these potential member stars are too low S/N to reliably measure any abundances. Stars 100 and 102 are known blue horizontal branch (BHB) member stars (Simon et al. 2015). Other than rejecting the clear nonmember star ID 191, we have avoided using metallicity information in

the membership selection so as to remain unbiased in final abundance distributions.

Note that several Ret II members have slightly lower μ_α and μ_δ than most of the galaxy (at $(\mu_\alpha, \mu_\delta) = (+2.0, -2.0)$ compared with $(+2.4, -1.3)$). These five stars were also offset in the same direction in Gaia DR2. However, they have larger proper motion uncertainties individually consistent with the bulk of the galaxy, and they do not stand out in radial velocity. Future Gaia data releases can test whether these represent a true feature.

3.4. Chemical Abundances

We derived most abundances using a standard analysis using 1D Castelli & Kurucz (2003) model atmospheres and local thermodynamic equilibrium (LTE) radiative transfer with MOOG (Sneden 1973) including scattering (Sobeck et al. 2011) and Barklem et al. (2000) damping.[22] Because Ba is the element of most interest, we analyzed Ba with both LTE and non-LTE, see Section 3.4.5. Our stellar parameters are given in Table 2, atomic data in Table 3, and abundance results in Table 4.

3.4.1. Stellar Parameters

Because our spectra cover a very small wavelength range with few lines, we determined effective temperatures for member stars from DES photometry and Dartmouth isochrones (Dotter et al. 2008). We adopted a 13 Gyr, [Fe/H] = −2.5, [α/Fe] = +0.4 isochrone as our fiducial isochrone. The isochrone was used to fit $T_{\rm eff}$ as a function of $g_0 - r_0$, and then we applied this to every member star. The brightest known member star (ID = 1) is near the DES saturation limit, with obviously incorrect r and i magnitudes in DES DR1. We adopted $g_0 - r_0 = 0.80$ from Simon et al. (2015) to determine this star's stellar parameters. Statistical uncertainties were calculated assuming a fixed error in $g_0 - r_0 = 0.02$ mag (the typical reddening uncertainty), resulting in a typical temperature error of 50–100 K. Systematic uncertainties were estimated by taking the largest difference between the fiducial isochrone and the $T_{\rm eff}$ calculated using isochrones of (12, 13, 14) Gyr, [Fe/H] = (−2.5, −2.0), and [α/Fe] = (0.0, 0.4), a typical uncertainty of 30–40 K. The total temperature uncertainty was the quadrature sum of these two uncertainties.

The surface gravity $\log g$ was determined photometrically using the equation $\log g = 4.44 + \log M_\star + 4 \log T_{\rm eff}/5780\mathrm{K} + 0.4(g_0 - \mu + BC(g) - 4.75)$ (Venn et al. 2017), where $M_\star = 0.75 \pm 0.1 M_\odot$ is the typical mass of an old red giant branch star, g_0 is the dereddened DES g magnitude, $\mu = 17.5$ is the distance modulus to Ret II, and $BC(g)$ is the Casagrande & VandenBerg (2014) bolometric correction. Besides the $M_\star$ and temperature uncertainties, we propagated a conservative 0.2 mag total uncertainty for the distance modulus and dereddening, as well as 0.03 mag uncertainty in the bolometric correction. The total $\log g$ uncertainty is about 0.2 dex for all stars. Using r instead of g led to the same $\log g$ within 0.05 dex, and using different metallicities for the bolometric correction led to differences within 0.02 dex.

The $T_{\rm eff}$ and $\log g$ in Table 2 agree with two previous works that studied a total of nine stars in Ret II using high-resolution spectroscopy (J16, R16). The stellar parameters in these two

---

[20] For two vectors x and y with covariance matrix Σ, $d_{\rm Mahalanobis} = \sqrt{(x-y)^{\rm T}\Sigma^{-1}(x-y)}$.
[21] We used the structural parameters from Mutlu-Pakdil et al. (2018), but the membership is the same using the structural parameters from Muñoz et al. (2018).
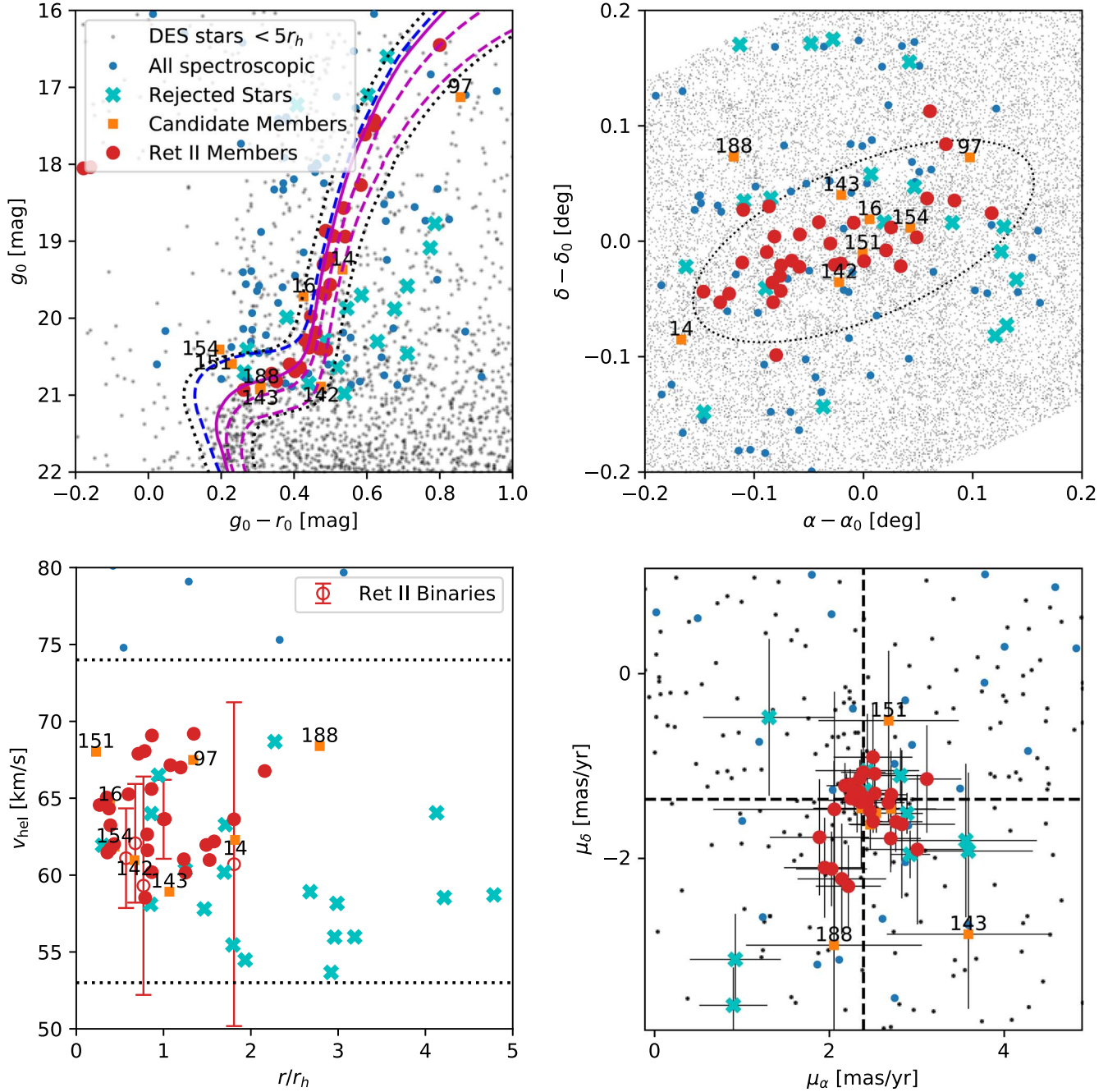
[22] https://github.com/alexji/moog17scat

Figure 2. Diagnostic plots for membership determination. Red circles indicate clear Ret II members, orange squares are candidate Ret II members (with star ID labeled), cyan crosses are nonmember stars with radial velocities similar to Ret II, small blue dots indicate spectroscopic targets with velocities far from Ret II, and small gray points indicate DES stars within five elliptical half-light radii. Top left: color–magnitude diagram with dereddened DES photometry. The solid magenta line is a Dartmouth 13 Gyr, [Fe/H] = −2.5 isochrone. The dashed magenta lines are more metal-rich 13 Gyr isochrones with metallicities [Fe/H] = −2.0 and −1.5. The dashed blue line is a 10 Gyr isochrone with [Fe/H] = −2.5 to show where potential younger member stars or blue stragglers could lie. The dotted black lines show the region for membership, though individual stars outside this range were also considered. Top right: spatial position of stars around the Ret II center, only including stars within five elliptical half-light radii. The dotted black line shows two half-light radii, which is used as the main membership cut, although stars at larger radii were also considered. Bottom left: radial velocity of spectroscopically observed stars vs. elliptical half-light radius. Binaries are indicated as open circles, with the error bar spanning the range of observed velocities. There is no significant radial velocity gradient. The dotted black lines show the range of velocities allowed for membership. Bottom right: Gaia EDR3 proper motions. All our spectroscopic targets are bright enough to have EDR3 proper motions. Stars 14, 16, 97, 142, and 154 are located at the center and thus not labeled. Note that the bulk of field stars are beyond the plot limits. The dashed black lines indicate the mean Ret II proper motion.

studies were derived using standard 1D-LTE methods, i.e., by balancing abundances of Fe lines with respect to excitation potential, ionization, and line strength, including a temperature recalibration to a photometric scale (Frebel et al. 2013). All nine stars agree within the 1σ stellar parameter uncertainties with no mean offset.

Our primary line of interest, the 6496 Å Ba line is saturated in essentially all of our stars with a detected Ba line. Microturbulence (ν_t) thus plays a major role in determining the final abundance and uncertainty, especially for the two coolest stars in our sample (IDs 1 and 97). Because we do not have enough lines to determine ν_t self-consistently in our stars,

Table 2
Stellar Parameters

ID	$T_{\rm eff}$	σ_T	$\log g$	σ_g	ν_t	σ_ν
1	4655	53	1.24	0.19	1.61	0.14
2	4952	49	1.85	0.18	1.48	0.13
3	4953	49	1.87	0.18	1.48	0.13
4	5009	49	1.95	0.18	1.46	0.13
5	5034	50	2.23	0.18	1.41	0.13
6	5157	68	2.41	0.19	1.39	0.13
7	5316	77	2.61	0.19	1.36	0.13
8	5146	67	2.56	0.19	1.36	0.13
9	5248	68	2.60	0.19	1.36	0.13
10	5256	68	2.61	0.19	1.36	0.13
11	5286	71	2.74	0.19	1.34	0.13
12	5331	82	2.79	0.19	1.34	0.13
13	5336	83	2.80	0.19	1.33	0.13
14	5166	69	2.74	0.19	1.34	0.13
15	5275	70	2.87	0.19	1.33	0.13
16	5564	83	3.06	0.19	1.31	0.13
17	5349	88	2.95	0.19	1.32	0.13
18	5320	77	2.94	0.19	1.32	0.13
19	5324	79	2.94	0.19	1.32	0.13
20	5481	92	3.13	0.20	1.30	0.13
21	5420	93	3.18	0.20	1.30	0.13
22	5492	91	3.26	0.19	1.29	0.13
23	5550	86	3.28	0.19	1.29	0.13
24	5499	91	3.30	0.19	1.29	0.13
25	5309	75	3.22	0.19	1.29	0.13
26	5915	88	3.60	0.19	1.27	0.13
97	4584	64	1.47	0.19	1.56	0.14
99	5379	95	3.25	0.20	1.29	0.13
134	5861	91	3.62	0.19	1.27	0.13
142	5363	90	3.44	0.20	1.28	0.13
143	6055	91	3.73	0.19	1.26	0.13
144	6263	113	3.81	0.20	1.26	0.13
151	6439	124	3.74	0.20	1.26	0.13
154	6645	130	3.73	0.20	1.26	0.13
157	5602	79	3.44	0.19	1.28	0.13
188	6046	92	3.72	0.19	1.26	0.13
192	5650	76	3.48	0.19	1.27	0.13
195	5704	87	3.47	0.19	1.27	0.13

Note. We adopt [M/H]$= -2.5$ and [α/Fe] $= +0.4$ for all stars.

we instead adopt a microturbulence relation based on $\log g$ from the metal-poor giants in Roederer et al. (2014):

$$\nu_t = 0.039(\log g)^2 - 0.331(\log g) + 1.960 \qquad (2)$$

where the typical scatter around the relation is 0.13 km s^{-1}. We note that this relation is quite different from the direct ν_t measurements in J16 and R16, but it eliminates a trend in Ba abundance with effective temperature that would otherwise be present. We have decided to adopt this relation for the rest of the main paper, and a complete investigation of microturbulence choices and the impact on our results is discussed in Appendices B and C.

Because we do not have Fe or α-element constraints for most stars, we assume everywhere a model metallicity of [M/H]$= -2.5$ and [α/Fe] $= +0.4$. We verified in stars with [Fe/H] and [Mg/Fe] measurements that changing these parameters produces negligible differences to the resulting abundances. The final stellar parameters and uncertainties for all members or candidate members are given in Table 2. We do not determine stellar parameters for the BHB stars (IDs 100 and 102).

Table 3
Atomic Data

λ (Å)	Species	χ (eV)	$\log gf$	Reference
		VLT		
6439.075	Ca I	2.524	0.390	SR81
6493.781	Ca I	2.521	-0.109	SR81
6494.980	Fe I	2.402	-1.273	BLA82
6496.897	Ba II	0.604	-0.380	GAL20
		M2FS Mg Wide		
5171.596	Fe I	1.484	-1.720	OBR91
5172.684	Mg I	2.712	-0.393	NIST
5183.604	Mg I	2.717	-0.167	NIST
5269.537	Fe I	0.858	-1.330	OBR91
5328.532	Fe I	1.556	-1.850	OBR91
5371.489	Fe I	0.957	-1.640	OBR91
		M2FS MedRes		
4554.03	56.1	0.000	$+0.17$	IVA06

References: SR81 (Smith & Raggett 1981), BLA82 (Blackwell et al. 1982), IVA06 (Ivans et al. 2006), GAL20 (Gallagher et al. 2020), OBR91 (O'Brian et al. 1991), NIST (Kramida et al. 2019), accessed through the Kurucz, VALD3, and linemake databases (Kurucz & Bell 1995; Ryabchikova et al. 2015; Placco et al. 2021).

3.4.2. VLT Data

In the VLT data, most Ret II member stars only have one to five significant absorption features: H-α, the Ba II line at 6496.897 Å, an Fe I line at 6494.98 Å, a Ca I line at 6439.08 Å, and sometimes a Ca I line at 6493.78 Å. We use these data to derive Ba, Fe, and Ca abundances where possible. Atomic data used are given in Table 3.

The Ba and Fe abundances are derived by fitting the spectral region from 6494−6504 Å. Given the systemic velocity of 64 km s^{-1}, the Ba line is right next to a strong and variable sky line at 6498.74 Å. The sky subtraction procedure described in Section 2 often leaves a significant residual (Figure 3). After testing several possible alternate sky subtraction procedures, we decided that the best course of action was to include the sky line residual in the model of this spectral region and marginalize over the uncertainty in our final results. For all member stars, a coarse normalization was first performed using a sigma-clipped third-order polynomial between 6450 and 6550 Å. We then excised a region of the spectrum from 6494 to 6504 Å to fit in detail. Our model of this region is an $8 + 4$ parameter model summarized in Table 5: a single Gaussian line width; six amplitudes for the Ca, Fe, and Ba stellar absorption features; a residual amplitude characterizing the sky line; a linear wavelength shift applied to the star but not the sky line; and a third-order polynomial to fit the residual continuum. Using the same line width for both stellar and sky features implicitly assumes that all lines were unresolved by the spectrograph, which is valid here. Note that the two lines at 6498.9 and 6499.7 Å are not present in any of the Ret II stars, but these were included in the model to fit more metal-rich foreground stars.

The model parameters were optimized using scipy.optimize.curve_fit. For five stars with high S/N (IDs 1, 3, 4, 5, 97), the best-fit χ^2 was larger than 1, suggesting that the data uncertainties were underestimated or that the model

Table 4
Abundances

ID	Mem	VLT S/N	M2FS S/N	[Mg/H]	σ_{Mg}	[Ca/H]	σ_{Ca}	[Fe/H]	σ_{Fe}	[Ba/H]$_{NLTE}$	σ_{Ba}	[Ba/H]$_{LTE}$	[Ba/H]$_{MR}$	$\sigma_{Ba,MR}$
1	M	140	...	...	...	−2.69	0.07	−2.89	0.10	−1.86	0.18	−1.58	−1.64	0.18
2	M	73	Mgb, 39	−2.48	0.12	−2.39	0.06	−2.76	0.09	−1.63	0.17	−1.33	−1.13	0.16
3	M	94	Mgb, 34	−2.59	0.13	−2.46	0.06	−2.77	0.08	−1.58	0.17	−1.28	−1.42	0.25
4	M	69	Mgb, 37	−2.55	0.11	−2.95	0.07	−2.66	0.19	−3.46	limit	−3.46	−0.83	limit
5	M	76	Mgb, 19	−2.52	0.13	−1.87	0.07	−2.02	0.13	−1.86	0.15	−1.57	−1.60	0.34
6	M	65	Mgb, 24	−2.75	0.13	−2.91	0.08	−3.18	0.12	−1.83	0.18	−1.54	−1.04	0.29
7	M	50	Mgb, 14	−2.67	0.22	−2.77	limit	−2.93	limit	−1.64	limit	−1.64	−0.83	limit
8	M	52	Mgb, 15	−2.03	0.16	−2.19	0.20	−2.14	0.15	−1.35	0.17	−1.12	−0.98	0.22
9	M	52	Mgb, 17	−2.72	0.13	−2.98	0.08	−2.89	0.14	−1.38	0.35	−1.08	−1.14	0.29
10	M	53	Mgb, 15	−2.09	0.18	−2.88	0.08	−3.28	limit	−3.41	limit	−3.41	...	...
11	M	...	Hα, 12	...	...	...	...	...	...	...	...	...	−1.14	0.37
12	M	39	Mgb, 15	−2.84	0.15	−2.69	0.11	−2.72	limit	−1.50	0.38	−1.20	−1.16	0.37
13	M	42	Mgb, 10	−2.60	0.16	−2.11	limit	−2.88	0.16	−1.64	0.22	−1.35	...	...
14	C	40	Hα, 10	...	...	−2.84	0.09	−3.14	0.20	−2.59	0.25	−2.53	...	...
15	M	34	Hα, 12	...	...	−2.64	limit	−3.07	limit	−2.83	limit	−2.83	...	...
16	C	30	Mgb, 10	...	...	−1.94	limit	−2.99	limit	−0.19	limit	−0.19	...	...
17	M	32	Hα, 12	...	...	−2.33	0.09	−2.60	0.21	−1.84	0.21	−1.63	−1.32	0.47
18	M	21	Hα, 12	...	...	−1.93	limit	−2.52	limit	+0.10	limit	+0.10	...	...
19	M	31	Hα, 12	...	...	−2.72	0.12	−2.66	0.21	−1.61	0.23	−1.35	−1.82	0.87
20	M	27	Hα, 5	...	...	−1.66	limit	−2.21	limit	+0.69	limit	+0.69	...	...
21	M	16	Hα, 7	...	...	−1.84	limit	−1.74	limit	−0.49	limit	−0.49	...	...
22	M	15	Hα, 5	...	...	−1.32	limit	−2.22	limit	−0.19	0.53	−0.21	...	...
23	M	19	Hα, 6	...	...	−1.52	limit	−2.00	limit	+0.79	limit	+0.79	...	...
24	M	19	Hα, 4	...	...	−1.23	limit	−1.86	limit	+0.46	limit	+0.46	...	...
25	M	20	Hα, 6	...	...	−2.38	0.20	−2.13	0.44	−0.56	0.56	−0.60	...	...
26	M	13	Hα, 4	...	...	...	limit	−2.21	limit	−1.55	0.27	−1.35	...	...
97	C	125	...	...	...	−2.36	0.11	−2.35	0.16	−1.84	0.17	−1.64	...	...
99	M	19	Hα, 7	...	...	...	limit	−2.30	0.27	−0.63	0.50	−0.60	...	...
100	M	...	Mgb, 25	...	...	...	...	...	...	...	...	...	...	...
102	M	...	Mgb, 28	...	...	...	...	...	...	...	...	...	...	...
134	M	13	Mgb, 2	...	...	−1.62	limit	−1.90	limit	+0.68	limit	+0.68	...	...
142	C	14	Mgb, 3	...	...	−1.89	0.23	−1.98	limit	−0.64	0.71	−0.68	...	...
143	C	10	Mgb, 3	...	...	−0.86	limit	−1.92	limit	−1.32	0.47	−1.04	...	...
144	M	11	Mgb, 2	...	...	−1.65	limit	−1.27	limit	−0.14	limit	−0.14	...	...
151	C	14	...	...	...	−1.58	limit	−1.64	limit	+0.36	limit	+0.36	...	...
154	C	13	...	...	...	0.34	limit	−0.37	limit	−0.34	0.61	+0.23	...	...
157	M	12	Hα, 5	...	...	−1.45	limit	−1.21	limit	+0.71	limit	+0.71	...	...
188	C	7	...	...	...	−0.26	limit	−1.09	limit	+0.30	limit	+0.30	...	...
192	M	17	Hα, 4	...	...	−1.65	limit	−2.11	limit	+0.12	limit	+0.12	...	...
195	M	14	Hα, 4	...	...	−2.22	limit	−2.02	limit	−1.56	0.37	−1.34	...	...

Note. In column "Mem," M indicates a clear member, and C indicates a candidate member. In the abundance uncertainty columns, "limit" means the indicated value is a 99% upper limit. [Ba/H]$_{NLTE}$ refers to our fiducial Ba abundances derived from MULTI/MARCS, [Ba/H]$_{LTE}$ is the Ba abundance derived from MOOG/ATLAS, and [Ba/H]$_{MR}$ is the MOOG/ATLAS abundance from the 4554 Å line derived from the medium-resolution M2FS observations.

did not provide a sufficient description of the data. For these stars, we increase the data uncertainties by 5%–30% such that the reduced χ^2 is 1. The other stars had reduced χ^2 of ≈ 0.8–0.9, but we leave their errors unscaled. Uncertainties in the fit were then found using dynamic nested sampling with `dynesty` (Speagle 2020). The priors used for the sampling are listed in Table 5. Every fit and Markov Chain Monte Carlo (MCMC) was visually inspected to ensure goodness of fit before accepting its results. Lines considered poor visual fits were marked for upper limit determination.

LTE abundances and uncertainties were determined by putting equivalent width distributions into curves of growth calculated by MOOG. First, the posterior distribution of the absorption line parameters were analytically converted into a posterior for the equivalent widths that marginalized over the effect of the sky line. Curves of growth were constructed with MOOG, which were used to convert the equivalent width

distribution to an abundance distribution. For Ba, the effect of hyperfine structure was included assuming an r-process isotope distribution (Ivans et al. 2006; Sneden et al. 2008). For detected lines, we adopt the optimum fit as the point estimate and larger of the difference between the point estimate and the 16th and 84th percentiles as a 1σ abundance error. For undetected lines, we adopt the 99th percentile of the abundance posterior as the upper limit. Despite this effort, stars with S/N < 25 still appear to have unreliable Ba abundances (Figure 3, Appendix B).

Stellar parameter uncertainties were found by calculating new curves of growth for 1σ differences in stellar parameters, redoing the above calculations, and taking the difference. These are added in quadrature to the statistical uncertainties.

As part of the above procedure, we fit the Ca line at 6493.8 Å. However, there is a stronger Ca line at 6439 Å that is more often detected and also less susceptible to non-LTE effects (Mashonkina et al. 2017). The Ca abundance is thus
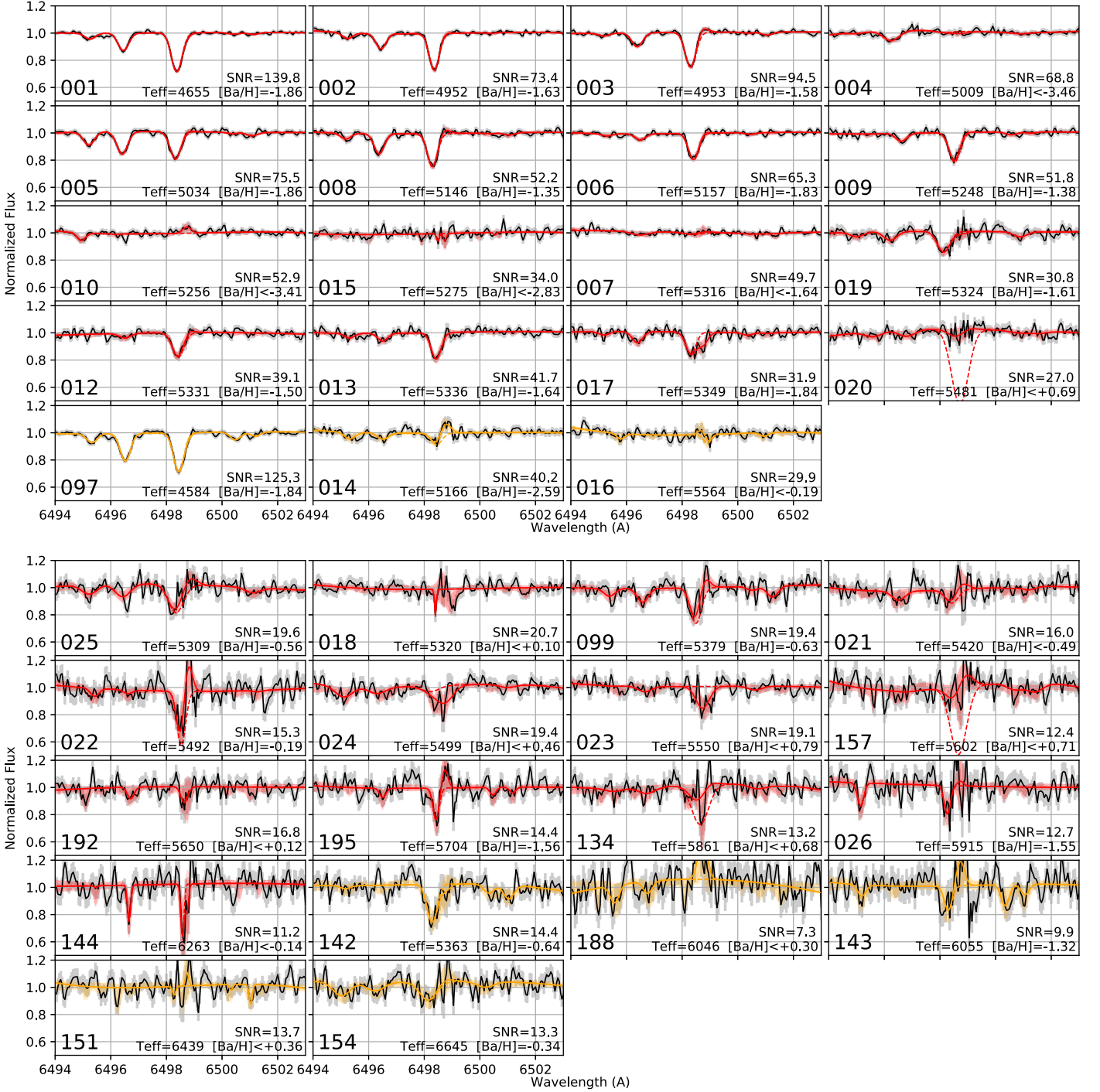
Figure 3. VLT spectra with best-fit models of the Ba line. From low to high wavelength the primary absorption features are due to Ca, Fe, and Ba. The Ba abundance measurement or limit is indicated. Stars are sorted by S/N, membership, and effective temperature. Top section: stars with S/N > 25. Bottom section: stars with S/N < 25. The sky residuals are clearly substantial for the lower S/N stars. The black line shows the data, while the gray shaded region indicates the 1σ spectrum noise. Best-fit models are shown in red and orange for clear and candidate members, respectively. The solid colored lines are the model including the sky line, while the dashed colored lines are the model fit in the absence of the fitted sky line residual. In some cases (e.g., stars 020, 134, 157) the Ba line is completely degenerate with the sky emission line, so no useful constraint is obtained. The shaded colored regions indicate the 16–84th percentile range of model parameters. Note that we have not explicitly plotted the upper limit model.

derived using this 6439 Å line with `smhr`. This includes the normalization, equivalent width measurement, and stellar parameter uncertainty propagation (Ji et al. 2020a). Formal 4σ upper limits for Ca were also calculated in `smhr` by synthesizing a Ca line such that $\Delta\chi^2 = 16$.

3.4.3. M2FS HiRes Abundances

We used `smhr` to normalize and stitch coadded orders, fit equivalent widths, measure element abundances from MOOG, and propagate stellar parameter uncertainties (see description in Casey 2014; Ji et al. 2020a). The primary use of these data is to

Table 5
VLT Spectrum Fit Parameters

Parameter	Description	Prior
A_{Ba}	Amplitude of 6496.9 Å Ba line	$\mathcal{U}[0, 1]$
λ_{Ba}	Observed wavelength of Ba line	$\mathcal{U}[6493.4, 6503.4]$
σ	Width of all lines	$\mathcal{U}[0.01, 0.30]$
A_{sky}	Amplitude of 6498.7 Å sky line	$\mathcal{U}[-0.50, 0.50]$
A_{Fe}	Amplitude of 6495.0 Å Fe line	$\mathcal{U}[0, 1]$
A_{Ca}	Amplitude of 6493.8 Å Ca line	$\mathcal{U}[0, 1]$
$A_{Fe,2}$	Amplitude of 6498.9 Å Fe line	$\mathcal{U}[0, 1]$
$A_{Ca,2}$	Amplitude of 6499.7 Å Ca line	$\mathcal{U}[0, 1]$
c_0	Constant Continuum Coefficient	$\mathcal{U}[0.5, 1.5]$
$c_{1,2,3}$	Continuum Coefficient	$\mathcal{U}[-1.0, 1.0]$

measure the Mg abundances, which we derive from equivalent widths of the Mg b lines at 5172 and 5183 Å. Useful abundances were ultimately only derived for the MgWide arm, because the BulgeGC1 arm only had fainter and warmer stars, and the 6496 Å Ba line was completely blended with a sky line.

3.4.4. M2FS MedRes Abundances

The primary line of interest in these data is the Ba 4554 Å line. We measure the abundance from this line with a procedure identical to that used for the VLT data, except that when fitting the equivalent width we manually define valid continuum wavelength ranges instead of modeling the many absorption lines. The results are provided in Table 4, and they are consistent with the Ba abundances derived from the 6496 Å line in the VLT data but with larger uncertainties. We thus do not use these abundances further. However, in the future this medium-resolution mode may be an efficient way to search for strong Ba lines in other UFDs.

3.4.5. Barium NLTE Abundances

Ba can be substantially affected by non-LTE effects (NLTE, e.g., Bergemann & Nordlander 2014; Mashonkina et al. 2014; Gallagher et al. 2020), especially when the lines are near saturation. For metal-poor giants, NLTE makes the Ba 6497 line stronger, resulting in lower inferred Ba abundances when including NLTE. To determine this quantitatively, we computed NLTE abundances for the Ba 6497 line using an updated version of the MULTI radiative transfer code (Carlsson 1986; Bergemann et al. 2019; Gallagher et al. 2020) and MARCS model atmospheres (Gustafsson et al. 2008). Like the MOOG/ATLAS analysis, we adopted a metallicity of $[M/H] = -2.5$ and $[\alpha/Fe] = +0.4$ for all model atmospheres, and used the model atom presented in Gallagher et al. (2020) including Barklem et al. (2000) damping. After precomputing a grid of NLTE curves of growth at many T_{eff} and $\log g$ values, we use Delaunay triangulation and linear interpolation to find NLTE abundances as a function of stellar parameters and equivalent widths (using scipy.interpolate.LinearNDInterpolator).

In the rest of this paper, we adopt the NLTE [Ba/H] abundances as our fiducial abundances. However, in Appendix C we show a comparison between the MOOG LTE/ATLAS and MULTI NLTE/MARCS abundances. Overall, the NLTE effects are approximately -0.3 dex, resulting in lower abundances compared with LTE modeling.

For completeness, we investigated NLTE corrections for Mg (Bergemann et al. 2017), Ca (Mashonkina et al. 2007), and Fe (Bergemann et al. 2012; Mashonkina et al. 2016).[23] We found that [Mg/H] increased by 0.06 ± 0.02 dex and [Ca/H] increased by 0.12 ± 0.04 dex, where the uncertainty indicates the variation across the stellar parameter range. For Fe, in most stars only the 6494.98 Å line is available to measure. Most NLTE correction grids do not include this line, with the exception of Mashonkina et al. (2016), whose interpolation grid only extends up to 5000 K. The correction for the three stars with $T_{eff} < 5000$ K increases [Fe/H] by 0.15 ± 0.01 dex. We decided not to include these corrections in our results, though these mean offsets can be applied if desired.

3.4.6. Abundance Summary

In summary, the main abundance results are Ba, Fe, Ca, and Mg measurements or upper limits. The VLT data are used to measure Ba, Fe, and Ca. The M2FS high-resolution data are used to measure Mg and to verify Fe and Ca. The M2FS medium-resolution data are used to verify Ba (Table 4). For the brightest stars, we use the M2FS HiRes data to derive abundances for Cr, Ti, and Nd, which we report in Appendix D. We do not discuss these elements more, as they are consistent with the discussion in J16 and R16. We adopt NLTE abundances for Ba and LTE abundances for other elements.

4. Results

4.1. Radial Velocity Distribution

Figure 4 shows the radial velocities of all stars in our sample (solid blue histogram). There is a clear peak at ≈ 65 km s^{-1} associated with Ret II. Stars considered clear Ret II members are shown as the solid red histogram, while all Ret II members, including candidates, are the open orange histogram (see Section 3.3 for details). For comparison, we show the radial velocity distribution of a smooth background halo from the Besançon model (Robin et al. 2003). We restrict the background to a CMD region surrounding our targets defined by four points $(g - r, g) = (0.2, 21.2), (0.7, 21.2), (0.45, 16.0)$, and $(1.0, 16.0)$. We query a large area for statistics and rescale the distribution to the FLAMES field of view.

The residual background after removing the clear and candidate members is shown as a purple histogram. There continues to be an excess of stars near the velocity of Ret II relative to the Besançon model. Detailed investigation of the proper motions and spatial position shows that these residual stars cannot be members of Ret II. There may potentially be additional structure in this region of the sky that is not part of Ret II, though we do not see any clear spatial or proper motion trends.

We determine the mean velocity $\bar{v}$ and velocity dispersion σ_v of Ret II with a Gaussian scatter model. Each star is assumed to have a true velocity distributed according to a Gaussian with mean and standard deviation $\bar{v}$ and σ_v, and the actual observed velocity has a Gaussian noise added to it with the individual velocity uncertainty in Table 1. The prior on the mean velocity is uniform with no bounds, and the prior on the scatter is uniform in log space from $\sigma_v \in [0.1, 10]$ km s^{-1}. The posterior

---

[23] Correction grids available at https://nlte.mpia.de/ and http://spectrum.inasan.ru/nLTE/.
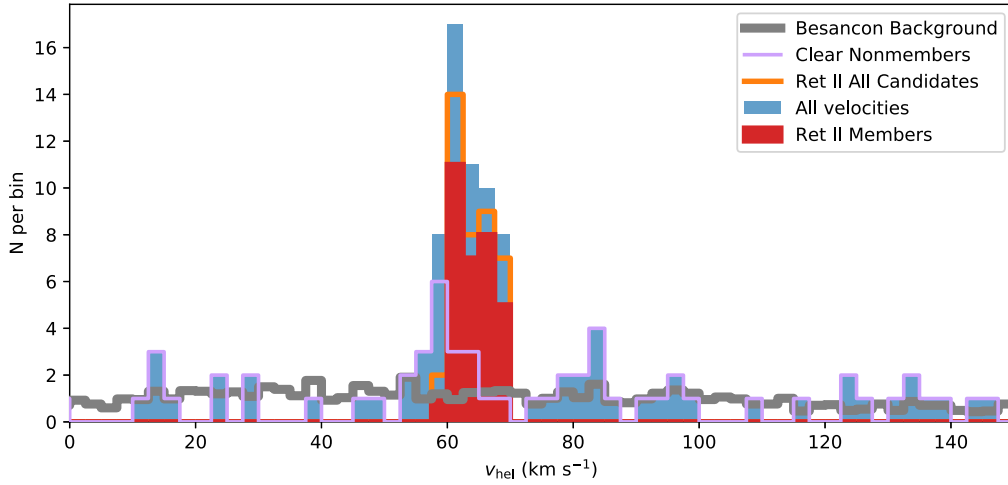
Figure 4. Histogram of measured velocities (blue), with definite (candidate) Ret II members in red (orange). For comparison, velocities from the Besançon model are shown as a gray histogram, normalized to match the observed sky area of 490 sq arcmin. The solid (dotted) purple histograms indicate subtracting the definite, red (candidate, orange) members from the full blue histogram. The nonmembers are overall consistent with the Besançon background model, though there is still a small excess above background near the velocity of Ret II.
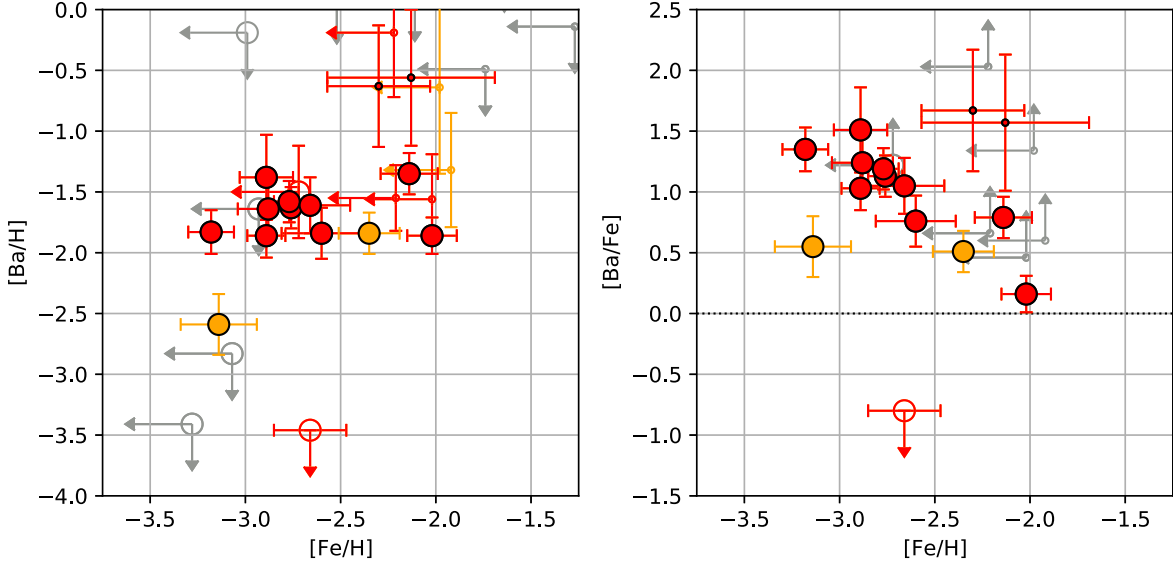
Figure 5. [Ba/H] and [Ba/Fe] vs. [Fe/H] as measured by VLT/GIRAFFE. Red points indicate clear Ret II members and orange points indicate candidate Ret II members. Large symbols are stars with S/N > 25, while small symbols are stars with S/N < 25. 1σ error bars are shown for all detected abundances, with arrows drawn to indicate upper/lower limits. Open circles indicate stars with at least one upper limit, and stars are colored gray if they have no detection of either Ba or Fe. Considering only the clear members with high S/N (large red points), there is no apparent scatter in Ba but significant spread in Fe.

is sampled using Stan (Carpenter et al. 2017, following Casey et al. 2021). All five likely binary stars are removed. Using only the 27 clear likely single members of Ret II, we obtain $\bar{v} = 63.9 \pm 0.5$ km s^{-1} and $\sigma_v = 2.97^{+0.43}_{-0.35}$ km s^{-1}. Adding the eight candidate members gives $\bar{v} = 64.0 \pm 0.5$ km s^{-1} and $\sigma_v = 2.96^{+0.44}_{-0.36}$ km s^{-1}, which is the same within the uncertainties. Our velocity dispersion is consistent both with previous measurements of ≈ 3.3 km s^{-1} (S15, W15, K15) and with the lower value of $2.8^{+0.7}_{-1.2}$ inferred by Minor et al. (2019), who statistically accounted for binaries. Our velocity dispersion is about two times more precise given more stars and additional independent velocity measurements, but we caution that our velocity dispersion uncertainties may be overly optimistic given the simple treatment of possible systematics (see Appendix A).

4.2. Abundance Trends

4.2.1. [Ba/H] versus [Fe/H]

Figure 5 shows the [Fe/H], [Ba/H], and [Ba/Fe] abundances of our sample. The red and orange points are clear and candidate Ret II members, respectively. Stars with limits on both [Fe/H] and [Ba/H] are shown in gray. Stars with S/N > 25 are shown as larger points, while stars with S/N < 25 are shown as smaller points. We only consider the large, high-S/N data points for the interpretation, but we show all the data for completeness.

There are two high S/N candidate member stars labeled on Figure 5. Star 97 is deemed a candidate member because it is extremely red compared with the fiducial Ret II CMD. Its low inferred metallicity of [Fe/H]$=-2.4$ is inconsistent with its
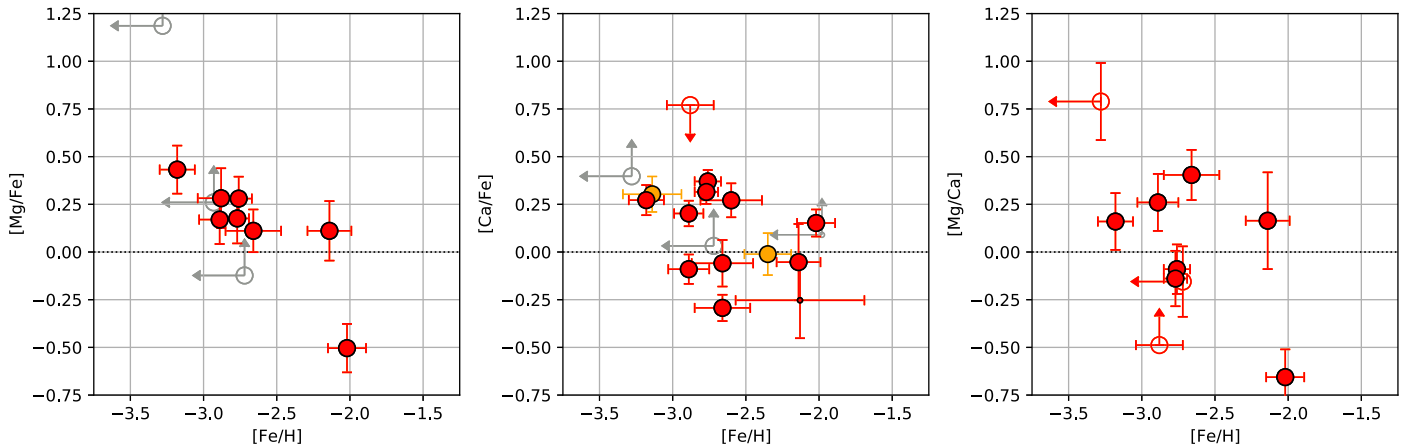
Figure 6. α-element abundances in Ret II. Symbols are the same as those in Figure 5, with large red solid points indicating abundances of confident members, large orange points indicating abundances of candidate members, open red points indicating stars with one upper limit, and open gray points indicating stars with two upper limits. Note that two stars have Mg and Ca measurements but only Fe upper limits. Left: [Mg/Fe] vs. [Fe/H]. Middle: [Ca/Fe] vs. [Fe/H]. Right: [Mg/Ca] vs. [Fe/H].

color unless it is an extremely carbon-enhanced star (e.g., Koposov et al. 2018). If it is a carbon-enhanced member, our model atmosphere grid may not be sufficient to accurately describe its properties. With this caveat in mind, the [Ba/H] for this star is right in line with most other Ret II stars. Star 14 is also deemed a candidate member due to its CMD position, which overlaps with a [Fe/H] = −1.5 isochrone. However, its weak Fe line suggests [Fe/H] ∼ −3.1. This clear inconsistency suggests either that it is a contaminant or that its spectrum cannot be modeled using photometric stellar parameters. We thus do not strongly consider either candidate member's Ba abundance.

It is clear that the majority (≈2/3) of high-S/N Ret II stars with meaningful Ba abundance measurements lie in a constant [Ba/H] plateau, while the minority (≈1/3) have low undetected Ba abundances. This corroborates the conclusions of Ji et al. (2016a), J16, and R16 that Ret II is enriched by a single prolific *r*-process event, but now with more than two times the number of *r*-process abundance measurements or upper limits. We note that for stars in the [Ba/H] plateau, there is a larger span in [Fe/H] than [Ba/H]. This is discussed in Section 5.

4.2.2. [α/Fe] versus [Fe/H]

We measure two α-elements, Mg and Ca, in several stars. The [α/Fe] versus [Fe/H] results are shown in Figure 6. The number of stars is low and the error bars are large, but the left two panels show that both [Mg/Fe] and [Ca/Fe] broadly decline with increasing [Fe/H]. Given the low statistics, there is no clear "α-knee" as seen in the Milky Way and some dwarf galaxies (Venn et al. 2004; Tolstoy et al. 2009; Hill et al. 2019), though we note that most dwarf galaxies do not have such a clear knee (Kirby et al. 2020; Theler et al. 2020). Regardless, both [Mg/Fe] and [Ca/Fe] show clear decreases somewhere between −3.0 < [Fe/H] < −2.5, a lower metallicity than the more massive classical dSph galaxies, as expected in a standard time-delay scenario (e.g., Frebel & Bromm 2012; Vargas et al. 2013).

While often assumed to vary together, in fact Mg and Ca can have different origins, because Mg is hydrostatically synthesized primarily in the most massive core-collapse supernova (CCSN) progenitors, while Ca is explosively synthesized in

most CCSN progenitors as well as SNe Ia (e.g., McWilliam et al. 2013; Hasselquist et al. 2017; Ji et al. 2020b). Most stars in Ret II have similar Mg and Ca abundances, with two notable exceptions. First, Star 5 has [Fe/H] ∼ −2.0 and very low [Mg/Fe] (as previously pointed out by J16). Second, Star 10 has [Fe/H] < −3 but a very high [Mg/Ca] = +0.8. These two stars drive an overall decreasing slope in [Mg/Ca] with respect to [Fe/H], which could (but does not have to) imply an early excess (and late-time lack) of the most massive CCSNe in Ret II. Ji et al. (2020b) pointed out that a decreasing [Mg/Ca] versus [Fe/H] trend is seen in several UFDs, but so far the trend is confined to UFDs that are kinematically associated with the Large Magellanic Cloud (LMC). An exciting possibility is that this indicates environment-dependent stellar populations or star formation histories. However, Ret II is likely only recently captured by the Large Magellanic Cloud (Erkal & Belokurov 2020; Patel et al. 2020, though see Battaglia et al. 2022).

Within the uncertainties, our Ca, Mg, and Fe measurements are consistent with previous results by J16 and R16. However, the lower S/N data in J16 suggested a broadly flat [Ca/Fe] trend, while our more precise and larger number of Ca measurements now clearly suggests an overall decreasing [Ca/Fe] trend with [Fe/H].

4.3. Intrinsic Scatter in [Fe/H]

We measure the intrinsic [Fe/H] scatter using the 13 definite member stars with [Fe/H] detections. The [Fe/H] distribution is modeled with a Gaussian (e.g., Li et al. 2018), and sampled using Stan in a manner similar to the velocity dispersion. We adopt a log-uniform prior for the intrinsic scatter of 10^{-2}–10^0. The results are a mean ⟨[Fe/H]⟩ = −2.64 with dispersion 0.32 dex, matching previous results (Koposov et al. 2015b; Simon et al. 2015; Walker et al. 2015). Adding Fe measurements from the two candidate members or including upper limits does not substantially affect these results.

4.4. Intrinsic Scatter in [Ba/H]

We detected [Ba/H] in 16 of our 32 member stars (21 out of 40 stars including candidate members). However, only [Ba/H] measurements from stars with S/N > 25 were considered
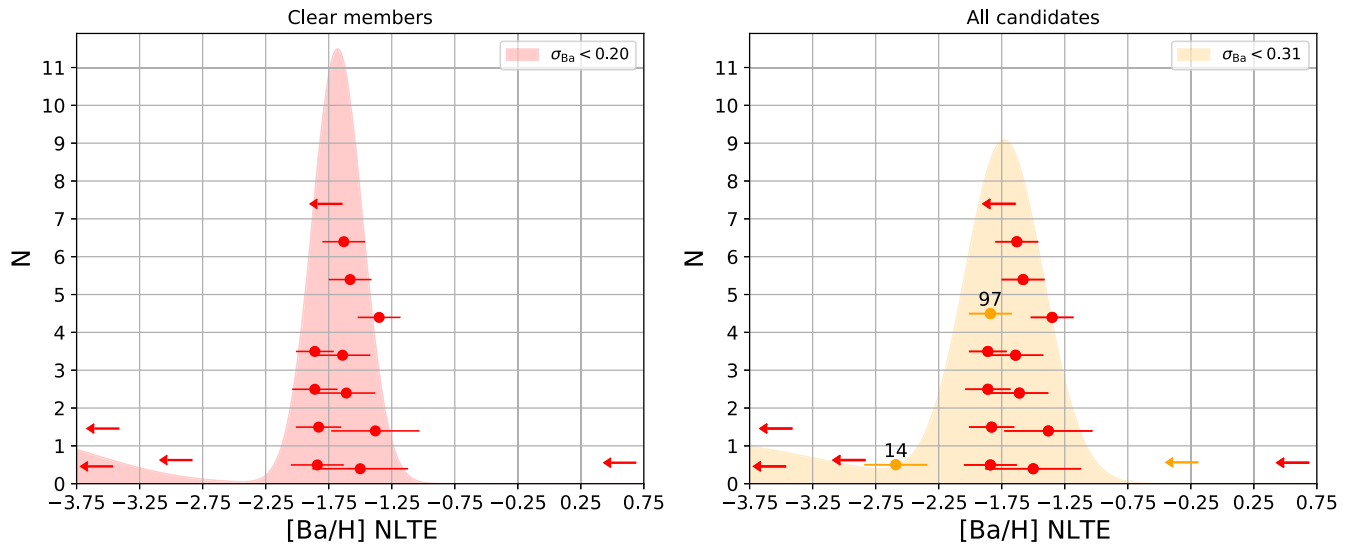
Figure 7. Barium measurements/upper limits and best-fit models for stars with S/N > 25. The left panel shows our fiducial result only including clear members (16 stars), while the right panel also includes candidate members (three more stars). Detections are shown as points with 1σ error bars, stacked within bins of 0.5 dex like a histogram. Stars with larger uncertainties are placed toward the bottom of each bin. Upper limits are shown as leftward-pointing arrows. Red and orange symbols indicate definite and candidate members, respectively. The shaded regions show the best-fit two-Gaussian model normalized to the number of stars on each panel. The width of both distributions (σ_{Ba}) is unresolved, so we plot the width using the 95% upper limit. Note that the model including candidates is wider primarily to accommodate Star 14.

reliable due to sky subtraction residuals (see Figure 3 and Appendices B and C), restricting the [Ba/H] measurements to 11 out of 16 member stars (13 out of 19 candidate members).

Figure 5 shows that the [Ba/H] measurements in Ret II have a clear peak at [Ba/H] ~ -1.7, and another group of stars with upper limits of [Ba/H] $\lesssim -3$ (as previously seen in Ji et al. 2016a; Roederer et al. 2016b [24]). We modeled this [Ba/H] distribution as a two-component Gaussian mixture. The model has five parameters: two means, two intrinsic dispersions, and a mixing fraction. We assume a log-flat prior for the intrinsic dispersions from 10^{-2}–10^{0}, a flat prior from 0 to 1 for the mixing fraction, and no constraint on the means (except that one has to be larger than the other). For the abundance likelihoods, for stars with [Ba/H] detections we used the usual Gaussian likelihood using the [Ba/H] measurement and uncertainty as the mean and standard deviation for that star. For the stars with [Ba/H] 99% upper limits, we adopted a step-function likelihood where 99% of the probability is uniform between [Ba/H] $= -5$ to the measured upper limit, and 1% of the probability is uniform from the measured upper limit to [Ba/H] $= +1$. This model was implemented in Stan and sampled using the No U-Turn Samplerwith four chains and 10^{6} steps. Model parameters were initialized near likely values from initial visual examination (i.e., mixing fraction based on the number of limits versus measurements, intrinsic scatters of 0.1 dex, and component means of -4.0 and -1.5). Our final chains were visually well mixed and had >10,000 effective samples for all parameters.

The results of our fiducial [Ba/H] dispersion fits are shown in Figure 7. Only stars with S/N > 25 are shown. The points show the exact [Ba/H] values and their uncertainties, and they are stacked in the vertical direction in bins of 0.5 dex like a histogram. As before, clear members are shown in red and candidate members in orange. The arrows indicate the 99% upper limits for stars with undetected Ba lines, which are

included in our modeling procedure. The best-fit two-component models are shown as shaded regions (red for clear members, orange for candidate members).

Overall, the detected Ba abundances for the clear member stars are clearly unimodal, and the per-star [Ba/H] uncertainty can explain the observed scatter in [Ba/H] abundances. We obtain a 95% upper limit $\sigma_{[Ba/H]} < 0.20$ dex. If adding the candidate members, we obtain a weaker upper limit $\sigma_{[Ba/H]} < 0.31$ dex, which is primarily driven by Star 14, which has a weak Ba line. As discussed previously, if this star is a member it is not likely that its stellar parameters can be determined with photometry, so the [Ba/H] inference for this star is likely inaccurate.

As a note of caution, we believe the choices made for our fiducial measurement are the most appropriate for quantifying the [Ba/H] intrinsic scatter in Ret II, as they minimize the impact from known systematic issues. But for completeness, in Appendix C we show the effect of all choices (i.e., S/N cut, membership, ν_t–$\log g$ relation) on the intrinsic scatter measurement. Changing the $\log g$–ν_t relation changes the limit to $\sigma_{[Ba/H]} < 0.28$ dex for clear members and $\sigma_{[Ba/H]} < 0.37$ dex for candidate members. This effect is driven almost entirely by the two cool stars (ID 1 and 97), which have low statistical uncertainty due to their brightness but have a strong dependence on microturbulence.

4.5. Abundance Trends with Radius

Figure 8 shows trends in [Fe/H], [Ba/H], [Mg/Fe], and [Ca/Fe] with radius for confirmed and candidate members. Overall, there are no strong abundance gradients for Fe and Ba. This lack of trend within this radius is expected, as any initial abundance gradients produced when Ret II was forming its stars at $z \gtrsim 6$ will likely be dynamically mixed away by $z = 0$: for 10^4 stars within the half-light radius of 58 pc and typical velocity of 3 km s^{-1}, the two-body relaxation time is about 2.5 Gyr (Binney & Tremaine 2008). Note that a metallicity gradient could be present at larger radii, as illustrated by the

---

[24] Star 7 has a much more stringent [Ba/H] upper limit in Ji et al. (2016a), but we kept its high [Ba/H] limit here to remain self-consistent.
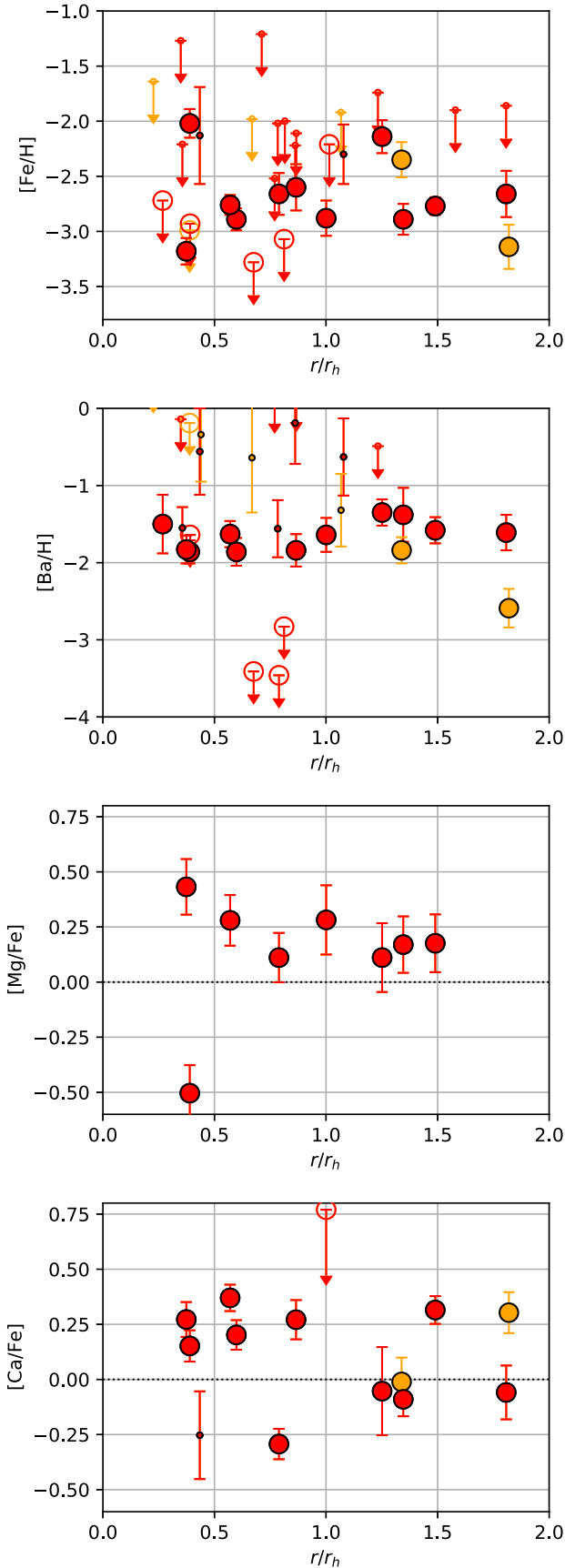
Figure 8. Abundance gradients. The *x*-axis on all plots is the elliptical radius, in units of the elliptical half-light radius. The symbols are as in Figure 5, with large red points indicating high-S/N stars with confident membership. There are no significant abundance gradients.

clear gradient in Tucana II (Chiti et al. 2021), but our observations only reach two half-light radii.

For Mg and Ca, there may be a small abundance gradient in [Mg/Fe] and [Ca/Fe], perhaps decreasing slightly at larger distances. For Mg, this could easily be due to small number statistics rather than an abundance gradient; for Ca, the scatter around a mean trend would be comparable to or larger than the size of the gradient itself. Thus, we do not consider there to be evidence for any abundance gradients out to two half-light radii.

5. Discussion

We have carefully determined the [Ba/H] distribution in Ret II. Figure 5 and 7 and Table 6 show that ~30% of the stars in Ret II are relatively metal-poor with no detected *r*-process elements, while ~70% of the stars in Ret II have identical *r*-process abundances of [Ba/H]= −1.7, precise to 0.2 dex. We now consider the implications of this measurement for galaxy formation and metal mixing (Section 5.1), the *r*-process site (Section 5.2), and chemical evolution in Ret II (Section 5.3). In most of the discussion we assume that the high [Ba/H] plateau in Ret II originates predominantly from a single *r*-process event. However, we consider (and dismiss) the possibility of Ba contamination from multiple *r*-process sources or non-*r*-process sources in Section 5.4.

Previous studies indicated that the *r*-process material in Ret II likely originates from a single *r*-process event, rather than multiple *r*-process events occurring within Ret II (Ji et al. 2016a; Roederer et al. 2016b). To update those conclusions with more recent results, out of 20 UFDs with high-resolution chemical abundances measured, Ret II has *r*-process abundances two to three orders of magnitude higher than the neutron-capture element abundances in other UFDs. It is thus extremely unlikely that Ret II would be enriched by multiple prolific *r*-process events, while other UFDs have no similarly prolific events. To estimate this probability, we ran Monte Carlo simulations assuming that the number of *r*-process events in each of 20 galaxies is distributed as a Poisson random variable. We assume each UFD is equally likely to host an *r*-process event and run simulations where the intrinsic rate of *r*-process events is between 0.00 and 0.50 events per galaxy. We then conservatively take the highest probability. The probability that any one galaxy gets $\geqslant 2$ *r*-process events while every other galaxy gets 0 *r*-process events is <1.5%. Two other ultrafaint satellites also appear to display a lower level of *r*-process enhancement (Tucana III and Grus II; Hansen et al. 2017, 2020; Marshall et al. 2018). If we assume that both of these systems are dwarf galaxies and hosted an *r*-process event, the probability that three UFDs have at least one *r*-process event and one has at least two *r*-process events is <6%. However, the classification of Tucana III and Grus II as dwarfs is currently uncertain (Simon et al. 2017, 2020); if neither is a dwarf galaxy then the probability of multiple *r*-process events in Ret II is again $\lesssim$1.5%. Thus, it is unlikely that Ret II was enriched by more than one *r*-process event.

5.1. Well-mixed [Ba/H] Implies Bursty Star Formation in Ret II

We first interpret the distribution of detected [Ba/H], which has a low intrinsic dispersion $\sigma_{\rm Ba} < 0.20$. Because all this *r*-process material is deposited at a single time in Ret II, the observed variation in [Ba/H] is entirely due to variations in

Table 6
Reticulum II Properties

Quantity	Value	Reference/Prior
R.A. (J2000)	03:35:47.83	Mutlu-Pakdil et al. (2018)
Decl. (J2000)	−54:02:47.8	Mutlu-Pakdil et al. (2018)
Position angle (deg)	68 ± 2	Mutlu-Pakdil et al. (2018)
Ellipticity	0.6 ± 0.1	Mutlu-Pakdil et al. (2018)
Half-light radius (arcmin)	6.3 ± 0.4	Mutlu-Pakdil et al. (2018)
Half-light radius (pc)	58 ± 4	Mutlu-Pakdil et al. (2018)
Distance modulus	17.5 ± 0.1	Mutlu-Pakdil et al. (2018)
Distance (kpc)	31.4 ± 1.4	Mutlu-Pakdil et al. (2018)
Heliocentric radial velocity (km s^{-1})	63.9 ± 0.5	Uniform
Velocity dispersion (km s^{-1})	$2.97^{+0.43}_{-0.35}$	$\log \sigma_v \sim \mathcal{U}[-1, 1]$
Mean metallicity $\langle$[Fe / H]$\rangle$	−2.64 ± 0.11	Uniform
Metallicity dispersion $\sigma_{[\mathrm{Fe/H}]}$	$0.32^{+0.10}_{-0.07}$	$\log \sigma_/ \sim \mathcal{U}[-2, 0]$
Mean NLTE barium abundance $\langle$[Ba / H]$\rangle$	−1.68 ± 0.07	Uniform
Barium dispersion $\sigma_{[\mathrm{Ba/H}]}$	$0.05^{+0.08}_{-0.03}$ or <0.20	$\log \sigma_/ \sim \mathcal{U}[-2, 0]$
Fraction of r-enhanced stars	$0.72^{+0.10}_{-0.12}$	$f_r = \mathcal{U}[0, 1]$
Absolute magnitude M_V	−3.1 ± 0.1	Mutlu-Pakdil et al. (2018)
Stellar mass $M_\star$ ($M_\odot$)	$10^{3.51 \pm 0.04}$	Assuming $M/L = 2.2$
Dynamical mass $M_{\mathrm{dyn},1/2}$ ($M_\odot$)	$10^{5.6 \pm 0.2}$	Using Wolf et al. (2010)

Note. Rows where the third column has a prior are measured from this work.

metal mixing. The unresolved Ba dispersion thus implies that the r-process material in Ret II must have been very well mixed by the time the high-Ba stars in Ret II formed. To interpret this homogeneous Ba, consider a parcel of gas with a fresh source of metals. There are two crucial timescales: τ_{mix}, the time for the metals to completely mix within that gas, and τ_{sf}, the time to turn that parcel of gas into stars. Stars forming from this gas will be chemically homogeneous if mixing is faster than star formation, i.e., $\tau_{\mathrm{mix}} < \tau_{\mathrm{sf}}$. The homogeneous Ba abundances in Ret II thus provide a lower limit on the time between when the r-process event occurs and when the next generation of stars forms. In other words, the mixing timescale provides a constraint on the burstiness of star formation. We argue in this section that both analytic estimates and simulations have shown that $\tau_{\mathrm{sf}} > \tau_{\mathrm{mix}} > 100$ Myr, and thus there must be at least a 100 Myr gap in the star formation history of Ret II. This is the first observational evidence of bursty star formation in an ultrafaint dwarf galaxy.

We first describe some basic physical ingredients determining τ_{mix}. Metal mixing in dwarf galaxies can be approximated as proceeding in two phases: the initial explosion remnant and subsequent turbulent mixing (e.g., Karlsson et al. 2008; Emerick et al. 2020). For an individual explosion, the initial remnant is dominated by a momentum-driven snowplow, lasts only $\sim 10^5$ yr, and sweeps up $\sim 10^5 M_\odot$ of gas (for a 10^{51} erg explosion; e.g., Cioffi et al. 1988; Ryan et al. 1996; Greif et al. 2007; Ji et al. 2015; Macias & Ramirez-Ruiz 2019; Magg et al. 2020). This mass is insignificant compared with a dwarf galaxy's interstellar medium (ISM). The dominant process determining τ_{mix} is thus turbulent mixing, where large-scale energy injection cascades to small-scale velocity eddies that enable microscopic diffusion (e.g., Pan et al. 2013). Turbulent mixing is typically modeled as a diffusion process (Klessen & Lin 2003; Karlsson et al. 2008; Greif et al. 2010; Ji et al. 2015; Krumholz & Ting 2018; Beniamini & Hotokezaka 2020; Tarumi et al. 2020), $R_t^2 \propto D_t \tau$, where R_t is the turbulent

diffusion distance, D_t is the turbulent diffusion coefficient, and τ is the time since material was deposited. Drawing an analogy to mixing length theory, the diffusion coefficient can be estimated by a typical length and velocity scale driving turbulence, $D_t \sim R_{\mathrm{turb}} v_{\mathrm{rms}}$. Complete mixing occurs when R_t reaches a length scale associated with the full size of the galaxy, $R_t = R_{\mathrm{gal}}$. Thus, $\tau_{\mathrm{mix}} \sim R_{\mathrm{gal}}^2 / (R_{\mathrm{turb}} v_{\mathrm{rms}})$ (Pan et al. 2013). In early dwarf galaxies, turbulence is primarily driven by gravitational gas accretion or mergers (Wise & Abel 2007; Greif et al. 2008; Klessen & Hennebelle 2010; Safranek-Shrader et al. 2012; Ritter et al. 2015), which can be used to estimate a turbulent diffusion coefficient (Karlsson et al. 2008; Ji et al. 2015). Putting in typical values for a dwarf galaxy ($R_{\mathrm{gal}} \sim 500$ pc the extent of the star-forming gas, $R_{\mathrm{turb}} \sim 100$ pc the size of a typical explosion remnant, and $v_{\mathrm{rms}} \sim 10$ km s^{-1} the turbulent velocity of ambient gas, from Tarumi et al. 2020) gives $\tau_{\mathrm{mix}} \sim 250$ Myr.

While intuitive, the mixing length formalism fails to describe the full physics of the complex, anisotropic, and multi-phase metal-mixing process in dwarf galaxies. For example, it is well known that mixing depends on the temperature of the ISM phase that the metals reside in, such that hot ISM phases mix much more efficiently than cold ISM phases (e.g., Kobulnicky & Skillman 1997; de Avillez & Mac Low 2002; Emerick et al. 2018, 2019, 2020), and the anisotropic topology of cold gas clumps and filaments in early dwarf galaxies affects where metals get deposited and new stars form (e.g., Webster et al. 2016; Chiaki et al. 2018; Magg et al. 2022). It is thus crucial to study metal mixing with hydrodynamic galaxy formation simulations. A few recent simulations have explicitly studied metal mixing in dwarf galaxies (e.g., Webster et al. 2014, 2015; Hirai et al. 2015, 2017; Revaz et al. 2016; Escala et al. 2018; Emerick et al. 2019, 2020; Tarumi et al. 2020; Jeon et al. 2021). In the vast majority of simulations, abundance scatter from individual metal sources is typically very large, ranging from 0.4 to 2.0 dex (e.g., Safarzadeh & Scannapieco 2017;

Emerick et al. 2020; Applebaum et al. 2021).[25] Note that many simulations compare their simulation abundance scatter directly with the observed abundance data, without deconvolving the abundance uncertainties.

Tarumi et al. (2020) performed a direct simulation of r-process enrichment in Ret II, simulating a UFD and injecting r-process elements from a single neutron star merger (NSM) to see the resulting r-process abundance spread. In order to homogenize the gas to a level consistent with that observed in Ret II, they found that the gas had to mix for a time period of a few hundred Myr before forming stars. They measure an effective diffusion coefficient in their simulation of $D_t \approx 10^{-3}$ kpc^2 Myr^{-1}, resulting in a complete mixing timescale of $\approx$250 Myr. Thus, we expect $100\,\mathrm{Myr} < \tau_{\mathrm{mix}} < \tau_{\mathrm{sf}}$, and the timescale between bursts of star formation in Ret II should be over 100 Myr, a significant fraction of a Hubble time at $z > 6$.

There are a few important caveats to the Tarumi et al. (2020) simulation. First, the mixing time can be affected by stochastic events. When Tarumi et al. (2020) exploded the NSM at the outskirts of the galaxy rather than the center (to mimic a velocity kick, also see Safarzadeh & Scannapieco 2017; Bonetti et al. 2019; Safarzadeh et al. 2019b), the lower diffusion coefficient resulted in less efficient mixing of the r-process elements. Emerick et al. (2019, 2020) also emphasize that the exact timing and location of r-process production relative to other stellar feedback sources that drive turbulence can both increase and decrease the mixing time. Second, the abundances in the Tarumi et al. (2020) simulation do not match Ret II observations: these simulations produce a flat trend in [Ba/Fe] versus [Fe/H], whereas Figure 5 shows a flat trend in [Ba/H] versus [Fe/H]. A correlation between Ba and Fe can occur if Ba and Fe are well mixed relative to each other but with varying overall metallicity differences. The simulations by Tarumi et al. (2020) indeed have a gas-rich merger that helps homogenize Ba and Fe but causes a dispersion in [X/H] at fixed time (Y. Tarumi, private communication). Finally, most galaxy formation simulations stay at relatively low resolutions, e.g., Tarumi et al. (2020), and adopt the ISM model from the Auriga Project that uses an effective equation of state model below 0.1 cm^{-3} (Grand et al. 2017). This may resolve mixing in the large-scale ISM, but it may not resolve small-scale inhomogeneous mixing (e.g., Pan et al. 2013; Chiaki et al. 2018; Magg et al. 2022). Tarumi et al. (2020) is the only simulation directly comparable to Ret II, but the overall timescale of >100 Myr to mix matches results from other simulations (Hirai et al. 2017; Emerick et al. 2019) and estimates based on the mixing length scaling relation (Karlsson 2005; Pan et al. 2013; Ji et al. 2015). Thus, the mixing timescale of >100 Myr seems robust.

In summary, the mixing time in UFDs is likely larger than 100 million years. The homogeneous r-process abundances in Ret II thus indicate that at least two early bursts of star formation occurred in Ret II, separated by at least a few hundred million years. The first burst produced r-process elements that enriched stars born in the second burst (which should be relatively extended due to the presence of Type Ia enrichment, see Section 5.3). Given that we find $\approx$70% of

Ret II stars are r-process enhanced, a concrete prediction is that star formation histories of Ret II with a precision of $\lesssim$100 Myr should show 30% of stars forming first, a gap of >100 Myr, and then the other 70% of star formation. Resolving bursty star formation on 100 Myr timescales is currently out of reach of direct star formation history measurements (e.g., Brown et al. 2014; Weisz et al. 2014a), but it qualitatively matches predictions from several UFD simulations (e.g., Jeon et al. 2017; Wheeler et al. 2019). These simulations achieve burstiness due to strong clustered supernova feedback, which purges the galaxy of star-forming gas and requires a long recovery time for gas to cool and form the next generation of stars (e.g., Jeon et al. 2014). The r-process elements can thus homogenize during this extended recovery time.

5.2. A Prompt, High-Yield R-Process Site

The [Ba/H] distribution in Ret II introduces some new constraints on the r-process site's yield and delay time. The mean $\langle[\mathrm{Ba/H}]\rangle = -1.68 \pm 0.07$ provides a constraint on the ratio $M_{\mathrm{Ba}}/M_{\mathrm{H}} = 136.5 \times 10^{[\mathrm{Ba/H}]-9.82} \approx 10^{-9.36}$, where 136.5 is the average atomic mass of Ba and $9.82 = 12.00 - 2.18$ accounts for the Asplund et al. (2009) solar composition. Assuming an r-process ratio of [Ba/Eu] = -0.80 in Ret II (Ji & Frebel 2018), this means $\langle[\mathrm{Eu/H}]\rangle = -0.88$, or $M_{\mathrm{Eu}}/M_{\mathrm{H}} = 152.0 \times 10^{[\mathrm{Eu/H}]-11.48} \approx 10^{-10.18}$, where 152.0 is the average atomic mass of Eu and $11.48 = 12.00 - 0.52$ accounts for the solar composition. The mass ratio M_{Eu}/M_r is $10^{-3.0}$, assuming M_r is elements with $A \geqslant 80$ from the solar r-process pattern (Sneden et al. 2008; Côté et al. 2018; Ji et al. 2019b). Thus, we find that $M_r/M_{\mathrm{H}} \approx 10^{-7.2\pm0.1}$, where M_{H} is an effective dilution mass of hydrogen.

Inferring the yield M_r of the r-process site depends on what is assumed for M_{H}. Ji et al. (2016a) previously argued that expected dilution masses range from 10^5–$10^7 M_{\odot}$. The lower end is set by the initial explosion remnant (also see simulations by Magg et al. 2022), and the upper end is set by the total available gas in a $10^8 M_{\odot}$ dark matter halo that is likely to host Ret II at high redshift. This would correspond to $M_r \sim 10^{-2.2}$–$10^{-0.2} M_{\odot}$. However, simulations show that the effective dilution masses are near the minimum of $10^5 M_{\odot}$ only when metals are inhomogeneously mixed (e.g., Chiaki et al. 2018; Jeon et al. 2021; Magg et al. 2022). The homogeneity of r-process elements in Ret II thus suggests that the metals have diluted into a larger hydrogen mass, which should be in the range 10^6–$10^7 M_{\odot}$. The higher dilution mass would imply a higher r-process yield of $M_r \sim 10^{-1.2}$–$10^{-0.2} M_{\odot}$.

An alternate way to estimate the r-process yield is to count up the amount of r-process elements locked into stars, then apply a correction factor for how much r-process material would not be captured in stars. A large fraction of r-process can be lost to the intergalactic medium due to the low gravitational potential of early dwarf galaxies (e.g., Beniamini et al. 2018; Brauer et al. 2021). Both empirically and theoretically, only $\lesssim 10^{-2}$ of metals are retained in dwarf galaxies (Dekel & Woo 2003; Robertson et al. 2005; Kirby et al. 2011; McQuinn et al. 2015). We can estimate the total mass of r-process in Ret II using its present-day stellar mass of $\approx$3300 $M_{\odot}$ (Mutlu-Pakdil et al. 2018). Assuming a hydrogen mass fraction of 0.75, the total r-process mass contained in Ret II today is $10^{-3.8} M_{\odot}$. Thus the expected yield of the r-process site should be $M_r \gtrsim 10^{-1.8} M_{\odot}$, consistent with our previous estimate $M_r \sim 10^{-1.2}$–$10^{-0.2} M_{\odot}$. Note that the dilution masses described

---

[25] Our scatter limit of 0.2 dex is a 1σ rms, for which almost no simulation provides a quantitative value. Because most UFDs in simulations are resolved by fewer than 100 star particles, we currently estimate the rms by taking the range of star particle abundances, which corresponds to $\pm 2\sigma$ interval, and dividing by 4. It would be helpful for future simulations to provide the actual rms values.

in Ji et al. (2016a) implicitly include this metal loss to the intergalactic medium (IGM), as the higher effective dilution masses can be thought of as corresponding to lower metal retention (also see Figure 11 of Magg et al. 2022).

The homogeneous [Ba/H] also suggests that the r-process site has to be fairly prompt in Ret II. Ji et al. (2016c) originally argued that the recovery times in UFDs (i.e., the time for gas to recollapse to the center of a halo after feedback) were longer than 10–100 Myr (Jeon et al. 2014; Ji et al. 2015; Bland-Hawthorn et al. 2015). This allowed a significant fraction of ordinary neutron star mergers with 10–100 Myr delay times to merge and enrich the gas before star formation. However, if the r-process material must then subsequently mix for an additional $\gtrsim 100$ Myr to homogenize, this puts strong pressure on the r-process site to be very prompt in order to mix fully before turning into stars. Additionally, Simon et al. (2022) recently obtained a precise star formation history for Ret II using Hubble color–magnitude diagrams. Combined with the result from this paper that 70% of Ret II stars are r-process enhanced, they concluded that the r-process time delay in Ret II must be shorter than 500 Myr.

Together, the higher r-process yield and more prompt r-process event implied by homogeneous r-process mixing slightly favor rare core-collapse supernovae over neutron star mergers as the source of r-process elements in Ret II. Our higher expected r-process yield of $10^{-1.2}$–$10^{-0.2} M_\odot$ is a better match to the 0.08–0.3 $M_\odot$ of r-process produced in collapsar disk winds (Fryer et al. 2006; Surman et al. 2006; Siegel et al. 2019; Miller et al. 2020), but is also consistent with magnetorotationally driven jets ($10^{-2.5}$–$10^{-1.5} M_\odot$ of r-process, Mösta et al. 2018) or neutron star mergers (10^{-3}–$10^{-1} M_\odot$, Wu et al. 2016; Radice et al. 2018; note GW170817 had r-process mass $\approx 10^{-1.5\pm0.3} M_\odot$, Chornock et al. 2017; Drout et al. 2017; Kilpatrick et al. 2017; Tanaka et al. 2017; Tanvir et al. 2017), or common envelope jet supernovae (e.g., Grichener & Soker 2019; Grichener et al. 2022). The fact that there is a few hundred Myr delay after r-process enrichment also favors core-collapse supernovae. However, very prompt and high-yield neutron star mergers are still on the table (Beniamini et al. 2016; Beniamini & Piran 2019; Safarzadeh et al. 2019a).

5.3. No Gas Accretion during Most Ret II Star Formation

Figure 5 shows that the [Ba/H] abundance of the r-process rich stars stays very flat over an extended range of [Fe/H]. This can be seen quantitatively by comparing the metallicity (Fe) dispersion of $0.32^{+0.10}_{-0.07}$ dex to the r-process (Ba) dispersion of <0.20 dex. The simplest interpretation of the larger Fe dispersion is that the r-process stars formed over some extended period of time where Ret II was able to self-enrich with iron from supernovae, as expected for a dwarf galaxy (Willman & Strader 2012). The flat [Ba/H] abundance would then clearly indicate that there is no pristine gas accretion nor any significant r-process production during the last 70% of Ret II's stellar mass growth. If there were significant pristine gas accretion during this time, it would reduce [Ba/H] at high [Fe/H].[26]

This gas cutoff scenario also could explain the [Mg/Ca] trend seen in Figure 6 through the integrated galactic initial

mass function (IGIMF; Weidner et al. 2013). In this model, a gas-poor galaxy is unable to create the densest and largest molecular clouds, introducing an effective upper mass limit to stars formed. Because Mg is predominantly produced in the most massive core-collapse supernovae and Ca is produced in all supernovae, a restricted gas supply will result in lower [Mg/Ca] abundances relative to a fully sampled IMF (McWilliam et al. 2013; Ji et al. 2020b; Lacchin et al. 2020). Thus, a lack of gas accretion could explain both the flat [Ba/H] and the declining [Mg/Ca] observed in Ret II. This observation should simplify chemical evolution models aiming to reproduce the r-process abundance trends of Ret II (e.g., Komiya & Shigeyama 2016; Ojima et al. 2018; Cavallo et al. 2021; Molero et al. 2021).

A lack of gas accretion may indicate something about the broader formation environment of Ret II. In particular, it is expected that UFDs like Ret II are ultimately quenched by reionization (e.g., Bullock et al. 2000; Benson et al. 2002; Brown et al. 2014; Rodriguez Wimberly et al. 2019), but it is not yet clear whether reionization immediately removes cold gas from halos or just restricts gas inflow (e.g., Okamoto et al. 2008; Weisz et al. 2014b; Jeon et al. 2017; Bose et al. 2018; Wheeler et al. 2019). Because >70% of Ret II stars form in the absence of significant gas accretion, it may be that it formed all these stars after reionization.

In this vein, it is interesting to note that Ret II is a satellite of the Large Magellanic Cloud (Erkal & Belokurov 2020; Patel et al. 2020; Battaglia et al. 2022). Sacchi et al. (2021) tentatively find that the star formation histories of LMC UFD satellites (including Ret II) take longer to complete the last 10% of their star formation history compared with Milky Way UFD satellites. This could suggest that LMC UFD satellites like Ret II were relatively isolated when they formed compared with Milky Way UFD satellites, and thus experienced delayed reionization. If so, it would support the concept of patchy reionization at the smallest galactic scales (e.g., Lunnan et al. 2012; Aubert et al. 2018). More recently, Simon et al. (2022) have determined the star formation history of Ret II with additional Hubble Space Telescope (HST) photometry. They find that Ret II likely took ~2.5 Gyr to form all its stars, largely corroborating the arguments from chemical evolution here.

For completeness, we note that the above discussion has implicitly assumed that τ_{mix} and τ_{sf} are the same for both Fe and Ba. One can imagine scenarios where the timing of stellar feedback causes an early source of Ba to be mixed more than a later source of Fe (e.g., Ritter et al. 2015; Schönrich & Weinberg 2019). In this case, stars at all metallicities would form simultaneously. This scenario seems unlikely for Ret II given the coherent evolution of Mg and Ca with [Fe/H], but it provides motivation to obtain more precise star formation histories in Ret II.

5.4. Contamination of Ba by Other Sources

We have interpreted our Ba measurements in Ret II as tracing pure r-process, based on the pure r-process patterns found in Ji et al. (2016a) and Roederer et al. (2016b). However, in principle there could be three possible contaminating sources of Ba that are empirically found in UFDs: (1) a low-yield source of Ba observed in most UFDs, of unknown origin (Frebel & Norris 2015; Roederer 2017; Ji et al. 2019c) but possibly attributed to r-process in neutrino driven winds (J16, Simon 2019) or s-process in rotating massive stars

---

[26] Tsujimoto et al. (2017) used a similar feature in Draco to argue for discrete r-process events, but in this relatively luminous galaxy there is a degeneracy between the number of r-process enrichment events and the presence/lack of gas accretion.

(Frischknecht et al. 2016; Limongi & Chieffi 2018; Tarumi et al. 2021); (2) late-time AGB enrichment in the ISM (Frebel et al. 2016; Ji et al. 2020b); or (3) mass transfer of *s*-process Ba from a binary companion (Frebel et al. 2014).

None of these possible contaminants will affect our conclusions. The impact of the first two sources is much less than the *r*-process content of Ret II, and it can be estimated by considering Ba abundances in other UFDs. The low-yield Ba source produces typical [Ba/H] ~ -4 (Ji et al. 2019c). Ba in the ISM from AGB stars is not often seen in UFDs given their short star formation durations, but where it is seen it reaches $[Ba/H]_{LTE} \sim -2.5$ (Frebel et al. 2016; Ji et al. 2020b). In both cases, the amount of contamination is at most 1/10 of the Ba in Ret II, too low to make a significant perturbation. For the third source, AGB mass transfer tends to produce [Ba/Fe] $\sim +2$, much more Ba than is observed in these stars (e.g., Frebel et al. 2014; Hansen et al. 2016). Thus, we find it extremely unlikely that Ba is tracing anything other than the single *r*-process event in Ret II.

However, we note that one candidate member, Star 97, is quite red both in DES and Gaia photometry. It is possible this is due to large amounts of carbon on the surface of the star, in which case it may have experienced mass transfer possibly including Ba. If so, this further justifies excluding Star 97 from our main results.

6. Conclusion

We have obtained multi-object spectroscopy of red giant branch members in the ultrafaint dwarf galaxy Reticulum II using VLT/GIRAFFE and Magellan/M2FS. Our redetermination of the velocity and metallicity dispersion is consistent with past results, and we detect no significant spatial gradients in the element abundances.

Ret II is of special interest due to its enrichment by a single *r*-process event. Our primary new result is a quantitative measurement of the [Ba/H] distribution (Figure 7, Table 6), which is a unique probe of gas dynamics and metal mixing within a faint, currently gas-free dwarf galaxy. Approximately 30% of Ret II stars have no detected *r*-process material, while the other 70% are enriched to a high enhancement. We place an upper limit of $\sigma_{[Ba/H]} < 0.20$ dex on the intrinsic [Ba/H] dispersion of the high-Ba stars, which implies that the initial *r*-process enrichment needs to turbulently mix and homogenize for at least 100 Myr before stars form. This is the first direct evidence of bursty star formation in a UFD. The long mixing time also favors an *r*-process site that is very prompt and produces a high *r*-process yield ($\gtrsim 10^{-1.5} M_{\odot}$). We thus slightly favor rare core-collapse supernovae as the source of *r*-process elements in this galaxy due to their higher *r*-process yield, though prompt high-yield neutron star mergers are allowed as well.

Examining the chemical evolution in Ret II, we find an overall declining [α/Fe] versus [Fe/H] pattern as expected in dwarf galaxies. Because [Ba/H] is flat over an extended [Fe/H] range, this suggests that Ret II did not accrete significant gas during the last 70% of its star formation. This is consistent with the observed declining [Mg/Ca] ratio if Ret II was too gas-poor to form the most massive core-collapse supernovae. The chemical evolution of Ret II thus suggests that it may have formed in an underdense environment, consistent with its status as a satellite of the Large Magellanic Cloud.

These constraints on UFD formation and the *r*-process site demonstrate the power of dwarf galaxy archeology. By finding stars in a common formation environment, it becomes possible to ask questions that could not be answered if these same stars were found individually scattered through the Milky Way. Reticulum II is unusually nearby and thus currently accessible for this type of study, but as the next generation of extremely large telescopes comes online, it will become possible to extend similar techniques to study the chemistry of ultrafaint dwarf galaxies throughout the Milky Way (Ji et al. 2019a).

Appendix A
Radial Velocities and Binarity

As a relatively nearby UFD of great scientific interest, Ret II has obtained many different epochs of radial velocities. We have collected all currently available literature velocities in Table 7. The literature velocities are mostly derived from coadding spectra taken across one to four adjacent nights, so the MJD reported here is only accurate to two days of precision. These velocities are not homogeneous and may suffer from systematic effects.

In a first attempt to calibrate the systematic effects, we adopt the S15 velocities as a reference velocity scale, as they have the most stars with common velocities compared with other literature sources. For matched stars in each sample, we calculate a weighted mean velocity offset. After removing this offset, stars with velocity variations inconsistent with a chi-squared test with $p < 0.01$ are identified as likely binaries (e.g., Chiti et al. 2022). We iterate this process until convergence, resulting in five binary stars: Stars 2, 13, 18, 19, and 21. The final mean velocity offsets relative to S15 are 1.01 km s^{-1} for K15, 0.63 km s^{-1} for J16, 1.02 km s^{-1} for Roederer et al. (2016b), 2.79 km s^{-1} for our VLT spectra, and 2.37 km s^{-1} for our HighRes M2FS spectra. Our MedRes M2FS data have a very large offset of -8.9 km s^{-1}, and we thus decided to exclude it from any velocity studies.

Table 7
Literature Radial Velocities

ID	v_{hel}	σ_{vhel}	v_{S15} MJD = 57072	σ_{S15}	v_{K15} MJD = 57090	σ_{K15}	v_{J16} MJD = 57298	σ_{J16}	v_{R16} MJD = 57341	σ_{R16}	v_{VLT} MJD = 58052	σ_{VLT}	v_{HR} MJD = 58073	σ_{HR}	v_{W15} MJD = 57072	σ_{W15}	v_{MR} MJD = 57639	σ_{MR}
1	+65.3	0.2	···	···	+66.3	0.2	+66.8	1.0	+65.5	1.0	+67.6	0.7	···	···	···	···	+56.3	2.4
2	+61.1	3.2	+59.1	0.9	+61.4	0.4	+62.7	1.0	+62.0	1.0	+65.5	0.7	+64.9	0.7	+61.8	0.4	+55.1	2.4
3	+62.0	0.4	+62.3	1.0	···	···	+62.0	1.0	+62.2	1.0	+63.5	0.7	+66.8	0.8	+63.2	0.5	+52.4	2.4
4	+58.5	0.3	+57.7	1.0	+59.6	0.5	+60.9	1.0	+59.7	1.0	+61.2	0.7	+60.4	0.8	+60.4	0.7	+47.3	2.4
5	+61.7	0.3	···	···	+63.5	0.5	+61.9	1.0	···	···	+63.8	0.7	+63.2	0.8	···	···	+54.0	2.4
6	+64.3	0.4	+64.4	1.1	+65.6	0.9	+63.5	1.0	···	···	+67.4	0.7	+67.0	0.8	+62.9	1.2	+59.7	2.4
7	+63.2	0.4	+65.2	1.2	+65.9	1.2	+62.7	1.0	···	···	+65.7	0.7	+65.0	0.9	+63.9	2.3	+43.6	2.4
8	+60.2	0.4	+59.8	1.2	+61.9	0.8	+61.9	1.0	···	···	+62.5	0.7	+61.7	0.8	+61.8	1.4	+51.6	2.4
9	+69.2	0.4	+69.7	1.4	+70.8	1.1	+71.6	1.0	···	···	+71.2	0.7	+70.8	0.8	+70.0	1.7	+59.6	2.4
10	+62.1	3.9	+62.3	1.1	+69.1	1.0	···	···	···	···	+64.0	0.7	+61.4	0.8	+65.6	1.1	···	···
11	+67.0	0.9	+67.9	1.1	+65.4	1.8	···	···	···	···	···	···	+70.2	3.2	+67.9	1.3	+61.3	2.4
12	+64.6	0.5	+65.7	1.1	+65.0	1.4	···	···	···	···	+67.2	0.7	+66.7	0.8	+69.1	1.5	+53.2	2.4
13	+63.6	2.6	+65.6	1.3	+68.2	1.7	···	···	···	···	+67.8	0.7	+63.1	0.8	+70.4	1.9	···	···
14	+62.3	0.7	+59.3	1.8	···	···	···	···	···	···	+65.3	0.7	+69.0	3.3	···	···	···	···
15	+62.6	0.6	+63.2	1.4	+63.4	1.7	···	···	···	···	+65.3	0.7	+65.1	3.3	+62.5	1.9	···	···
16	+64.6	0.9	+59.1	8.2	···	···	···	···	···	···	+67.4	0.9	+0.0	0.0	···	···	···	···
17	+60.2	0.7	+57.4	2.4	+60.0	2.1	···	···	···	···	+63.3	0.7	+64.9	3.3	+60.1	2.1	+40.7	2.4
18	+59.3	7.1	+66.3	1.4	+62.9	3.7	···	···	···	···	+59.4	0.8	+73.6	3.3	···	···	···	···
19	+60.7	10.5	+67.9	1.4	+78.9	1.8	···	···	···	···	+57.9	0.8	+64.4	3.3	+70.2	3.3	+26.5	2.4
20	+63.6	0.7	+63.5	1.4	···	···	···	···	···	···	+66.3	0.7	+70.9	3.4	+66.4	2.9	···	···
21	+61.0	0.8	+56.7	1.9	···	···	···	···	···	···	+64.7	0.9	+64.2	3.4	···	···	···	···
22	+65.6	0.7	+64.7	1.8	···	···	···	···	···	···	+68.6	0.8	+68.4	3.5	+66.7	2.0	···	···
23	+61.6	0.7	+59.8	1.8	···	···	···	···	···	···	+64.7	0.8	+65.2	3.5	···	···	···	···
24	+63.6	0.8	+68.0	3.5	···	···	···	···	···	···	+65.9	0.8	+71.6	3.4	···	···	···	···
25	+62.0	0.7	+61.9	2.0	···	···	···	···	···	···	+64.9	0.8	+63.0	3.4	+65.0	2.9	···	···
26	+61.5	0.8	+61.7	4.8	···	···	···	···	···	···	+64.0	0.9	+69.1	4.0	···	···	···	···
97	+67.5	0.7	···	···	···	···	···	···	···	···	+70.3	0.7	···	···	···	···	···	···
99	+67.2	0.8	···	···	···	···	···	···	···	···	+69.9	0.8	+70.9	3.8	···	···	···	···
100	+61.0	0.8	···	···	···	···	···	···	···	···	···	···	+63.4	0.8	···	···	···	···
102	+66.8	0.7	···	···	···	···	···	···	···	···	···	···	+69.1	0.7	···	···	···	···
134	+62.2	1.0	···	···	···	···	···	···	···	···	+65.0	1.0	+0.0	0.0	···	···	···	···
142	+61.0	0.7	···	···	···	···	···	···	···	···	+64.0	0.9	+63.0	1.1	···	···	···	···
143	+58.9	0.9	···	···	···	···	···	···	···	···	+61.7	0.9	+0.0	0.0	···	···	···	···
144	+65.0	1.1	···	···	···	···	···	···	···	···	+67.6	1.2	+68.5	2.6	···	···	···	···
151	+68.0	1.0	···	···	···	···	···	···	···	···	+70.8	1.0	···	···	···	···	···	···
154	+61.9	1.0	···	···	···	···	···	···	···	···	+64.6	1.0	···	···	···	···	···	···
157	+67.9	0.9	···	···	···	···	···	···	···	···	+70.5	0.9	+73.1	3.4	···	···	···	···
188	+68.4	1.2	···	···	···	···	···	···	···	···	+71.2	1.2	···	···	···	···	···	···
192	+69.1	0.9	···	···	···	···	···	···	···	···	+72.2	0.9	+66.9	3.5	···	···	···	···
195	+68.1	0.8	···	···	···	···	···	···	···	···	+71.1	0.8	+65.2	4.2	···	···	···	···

Appendix B
Effect of Microturbulence on Barium Abundances

Microturbulence (ν_t) is a parameter introduced to 1D stellar atmospheres to account for unmodeled 3D atmospheric effects. It affects lines at the saturated part of the curve of growth, where a higher microturbulence effectively desaturates strong lines by adding some extra doppler broadening (e.g., Gray 2008). When lots of Fe I lines are available, microturbulence is usually found by balancing Fe I abundance as a function of line strength. Empirical measurements of microturbulence show that red giants with lower surface gravities (and temperatures) tend to have higher microturbulence values (e.g., Barklem et al. 2005).

In our VLT spectra, the Ba 6496 Å line is at or near saturation when detected. For our coolest giants, increasing ν_t by 0.2 km s^{-1} reduces [Ba/H] by 0.15 dex. Because we aim to resolve abundance scatter on the order of 0.20 dex, this systematic effect is often the dominant uncertainty, especially for the brightest giants where the equivalent width is well measured. There are not enough Fe lines to self-consistently measure ν_t in our stars, so we must use existing correlations between $\log g$ and ν_t. Here, we investigate five different data sets that measured ν_t using high-resolution spectroscopy of metal-poor red giant stars, examining systematic differences in ν_t–$\log g$ relations, as well as the scatter around those relations. The effect of these choices on our barium abundance results is investigated in Appendix C.

Figure 9 shows the result of our investigation. The left column in Figure 9 plots $\log g$ versus ν_t for data from Barklem et al. (2005; B05), Marino et al. (2008; M08), Cohen et al. (2013; C13), Roederer et al. (2014; R14), and Jacobson et al. (2015; J15), while the other columns show the measured [Ba/H]$_{\rm LTE}$ compared with $T_{\rm eff}$, [Fe/H], and the S/N. We separate Roederer et al. (2014) into a giants-only sample as well (R14g). When available, we use the stellar parameters as tabulated in JINAbase (Abohalima & Frebel 2018). Horizontal branch stars have higher microturbulence than RGB stars, so they are removed with a cut $\log g > 0.00286 T_{\rm eff} - 12.7$. To each data set, we fit a linear and quadratic polynomial for ν_t as a function of $\log g$, using a robust fitter based on the routine `robust_poly_fit` in the AstroIDL library. The scatter around the fit is measured with the biweight scale of the residuals (a robust standard deviation). The coefficients and scatter around each relation are given in Table 8.

Note that the right column of Figure 9 shows that our stars with S/N < 25 have a much larger scatter than stars above that threshold. Visual examination of the spectra (Figure 3) suggests that these stars are adversely affected by inaccurate sky subtraction that is blended with the Ba line. We thus have decided to exclude the low-S/N stars from most analyses. Also note that we used MOOG LTE/ATLAS [Ba/H] abundances for this figure, though the conclusions are robust if using NLTE instead.

B.1. Mean Relations

There are clear differences in the average ν_t–$\log g$ relation across different literature samples: at low $\log g$, the first three rows (B05, C13, J15) have systematically higher ν_t than the last three rows (M08, R14, R14g). The origin of this difference is not clear. One possibility is the spectra for M08 and R14 have S/N ∼ 100, substantially higher than B05 and J15, which typically have S/N ∼ 30. The low S/N of weak iron lines could bias microturbulence too high (as described by Magain 1984). However, C13 also have S/N ∼ 100 and obtain higher microturbulence values. Another possibility is that NLTE effects bias the microturbulence due to underlying correlations between excitation potential, line strength, and typical NLTE correction size (Bergemann et al. 2012). Further investigation of these differences would be valuable but is beyond the scope of this paper's appendix.

In this paper, we have decided to pick a ν_t–$\log g$ relation that leaves no trend in the [Ba/H] and $T_{\rm eff}$ for our stars. In Figure 9, the second column shows [Ba/H] versus $T_{\rm eff}$, where the first three rows of Figure 9 have a strong systematic trend such that cooler stars have lower [Ba/H]. The bottom three rows do not have a significant trend. The coolest stars have the highest S/N and lowest statistical uncertainty, so the different mean trend makes a significant difference on our final inferred Ba scatter. Figure 10 shows this specifically for the high S/N and clear member stars for the R14g and B05 relations. The R14g ν_t–$\log g$ relation clearly has less trend with $T_{\rm eff}$ than B05. Note that the trends are primarily driven by the two coolest and brightest stars ($T_{\rm eff} \sim 4500$ K). Because these two stars have low statistical uncertainty on their [Ba/H] abundances, the systematic effect of microturbulence can make a large difference in the inferred [Ba/H] scatter.

We have decided to adopt the quadratic ν_t–$\log g$ relation from the giant stars in Roederer et al. (2014; R14g) as our fiducial results. R14g have the highest S/N spectra of metal-poor giants with the largest wavelength coverage out of all these data samples. The results of this paper would not change if we used the very similar M08 or R14 relations instead. However, this ν_t–$\log g$ relation is different from most previous studies of dwarf galaxy stellar abundances (Ji et al. 2016b; Roederer et al. 2016b; Ji & Frebel 2018). Thus, in Appendix C we give all results using the ν_t–$\log g$ relation from B05 as well, which matches those previous abundance studies. We note that adding NLTE effects for Ba exacerbates the trend for [Ba/H] versus $T_{\rm eff}$ when using the B05 ν_t–$\log g$ relation, because the NLTE corrections are larger (more negative) when microturbulence is higher. It is also worth noting that past studies of Ret II had clear [Ba/H] trends with temperature that can be explained by microturbulence.

B.2. Microturbulence Scatter

Typically, a systematic uncertainty of ≈0.2 km s^{-1} is adopted for microturbulence, which accounts for the systematic mean differences described above. However, because we are interested in the abundance scatter within Ret II, another crucial value is the *intrinsic scatter* in microturbulence around a "true" ν_t–$\log g$ relation, i.e., changes in the atmospheric structure that are unmodeled by $\log g$ alone. This error is likely *smaller* than the observational scatter, because the microturbulence measurements themselves are noisy.

Examining our five data sets, two have a scatter of ∼0.2 km s^{-1} (C13, J15), while three have a scatter of ∼0.1 km s^{-1} (B05, M08, R14). Using a smaller intrinsic ν_t scatter would increase the significance of our scatter detections, while a larger intrinsic ν_t scatter reduces the significance. Because we have adopted the mean ν_t–$\log g$ relation from R14g, we also decide to adopt the intrinsic scatter of 0.13 km s^{-1} from that data sample. In our systematic
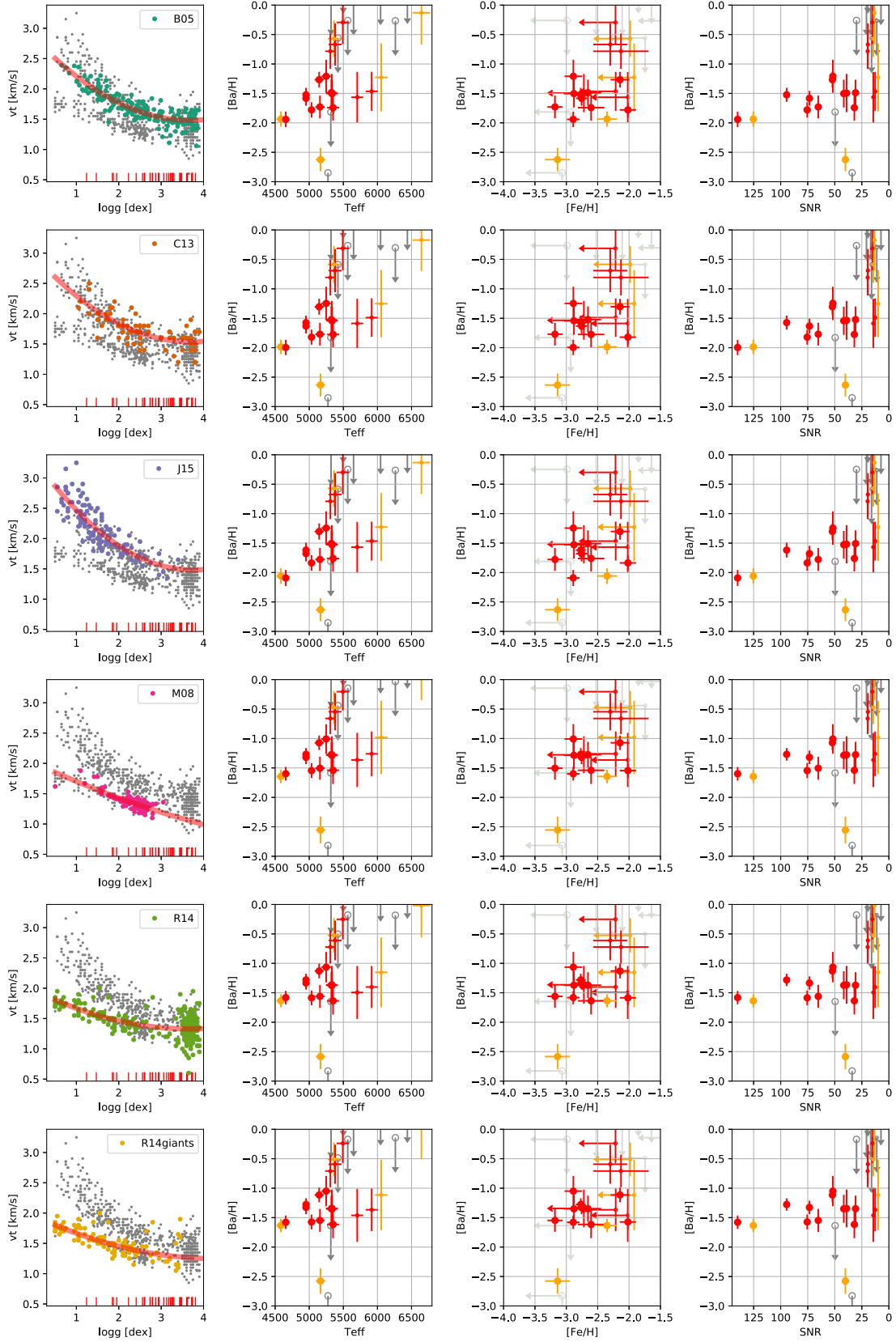
Figure 9. Impact of different $\nu_t - \log g$ relations. Left column: $\log g$ vs. ν_t for each sample of stars. The thin red lines at the bottom indicate the $\log g$ of Ret II stars. The best quadratic fit is plotted as a thick red line. The gray points show stars from all other rows for context. Left-middle column: [Ba/H] vs. T_{eff}. Right-middle column: [Ba/H] vs. [Fe/H]. Right column: [Ba/H] vs. S/N. Stars with S/N < 25 display substantially larger [Ba/H] scatter, likely due to residuals from sky subtraction. Overall, the first three rows (B05, C13, J15) have similar trends, showing an upturn in ν_t at low $\log g$ but a very noticeable trend in [Ba/H] vs. T_{eff}. The last three rows have smaller ν_t and little trend in [Ba/H] vs. T_{eff} (excluding stars with S/N < 25).
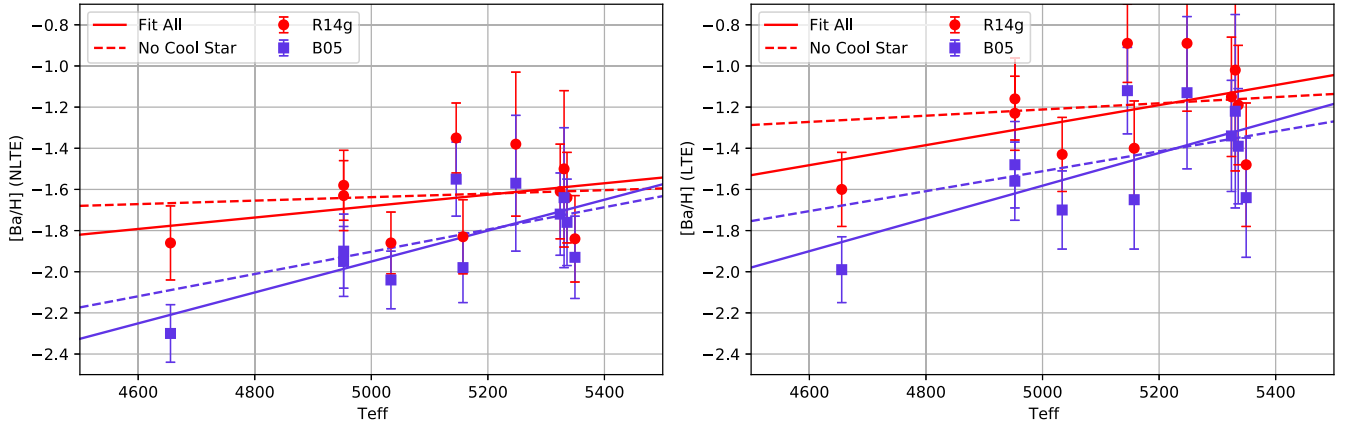
Figure 10. Comparison of [Ba/H] vs. $T_{\rm eff}$ slopes for different microturbulence relations. In contrast to Figure 9, here we only include the high S/N clear member stars. The left and right panels show the NLTE and LTE [Ba/H] abundances, respectively. The red circles and blue squares indicate [Ba/H] derived using the R14g and B05 $\nu_t-\log g$ relations, respectively. The red and blue solid lines indicate a fit to all stars using the R14g and B05 relations, respectively, while the dashed lines indicate the fit removing the coolest star (ID 1). It is clear that the trend with $T_{\rm eff}$ is flatter using the R14g relation, regardless of whether the coolest star is included. For the NLTE panel, the slopes of the lines (in units of dex per 100 K) are 0.03 and 0.08 for R14g and B05, respectively, or 0.01 and 0.05 when removing the cold star for R14g and B05, respectively.

Table 8
Fit Parameters for ν_t

Sample	Quadratic Fit	σ	Linear Fit	σ
B05	$0.1001 \log g^2 + -0.7394 \log g + 2.847$	0.12	$-0.2527 \log g + 2.316$	0.15
C13	$0.1048 \log g^2 + -0.7744 \log g + 2.965$	0.18	$-0.2189 \log g + 2.300$	0.20
J15	$0.1307 \log g^2 + -0.9812 \log g + 3.322$	0.21	$-0.5217 \log g + 2.973$	0.22
M08	$0.0175 \log g^2 + -0.3242 \log g + 2.009$	0.08	$-0.2545 \log g + 1.944$	0.08
R14	$0.0471 \log g^2 + -0.3474 \log g + 1.969$	0.18	$-0.1201 \log g + 1.764$	0.18
R14 giants	$0.0386 \log g^2 + -0.3313 \log g + 1.960$	0.13	$-0.2247 \log g + 1.897$	0.10

investigations using the B05 sample, we adopt the corresponding intrinsic scatter of 0.12 km s^{-1}.

Appendix C
Systematic Effects on Barium Scatter

Here we explore the effect of different data subsets and microturbulence relations on the main result of this paper, the [Ba/H] mean and scatter. For the data samples, we consider permutations of membership (clear members only versus including candidate members) and MULTI NLTE/MARCS versus MOOG LTE/ATLAS. For the microturbulence relations, we use the fiducial R14 giants (R14g) relation, as well as the B05 relation, which has a higher microturbulence for the coolest/lowest gravity giants. For each of these permutations, we fit the two-component Ba scatter model described in Section 4.4. Note that while our fiducial model is run with a very large number of steps, for the other models we only sampled to reach $\gtrsim$100 effective samples, and thus the uncertainties and limits on the parameters will be less accurate.

Table 9 gives the results of the model fits. The first row is our fiducial value, while the other rows show various data permutations. μ_1 and σ_1 are the most important values, indicating the mean and intrinsic spread on the detected [Ba/H] abundances. μ_2 and σ_2 are the mean and scatter of the undetected [Ba/H] component, which is not well constrained given that no low [Ba/H] abundances were detected. p_2 is the fraction of stars in the undetected [Ba/H] component, i.e., $1 - p_2$ is the fraction of r-enhanced stars. The uncertainties are 1σ, and the limit on σ_1 is a 95% limit.

We point out three main conclusions of Table 9. First, the MULTI NLTE/MARCS mean [Ba/H] abundances (μ_1) are typically lower than the MOOG LTE/ATLAS abundances by about 0.3 dex. Figure 11 shows that the typical [Ba/H] correction going from MOOG to MULTI is -0.27 ± 0.04 dex in a way that is fairly close to a constant offset. This is a result of both the different model atmospheres as well as the effect of NLTE. Second, when considering just the clear member stars, none of the models detects a significant [Ba/H] dispersion σ_1. The constraint is stronger when using NLTE, but weaker when using the B05 microturbulence relation instead of the R14g microturbulence relation. This is driven primarily by the coolest Ret II star (ID 1), which is most affected by the different microturbulence relations (Figure 9). Third, when including the candidate member stars, all the upper limits on σ_1 get looser, and actually in one case (B05 MOOG with candidates) the intrinsic dispersion is resolved at 2σ. This is predominantly because of the outlier Star 14, which has a weak but detected Ba line. If this star is actually part of Ret II, then our two-component model for [Ba/H] is likely insufficient to describe the data because Star 14 is well outside the main peak of [Ba/H] detections, but well above the more stringent [Ba/H] upper limits.

After examining Table 9 and Figure 9, we decided that using the R14g MULTI/NLTE results with only clear members is the most reliable measurement. It is clear that using NLTE and definite members will result in a better measurement, and eliminating the trend with stellar parameters discussed in Appendix B justifies using R14g instead of B05. However, for completeness, we show
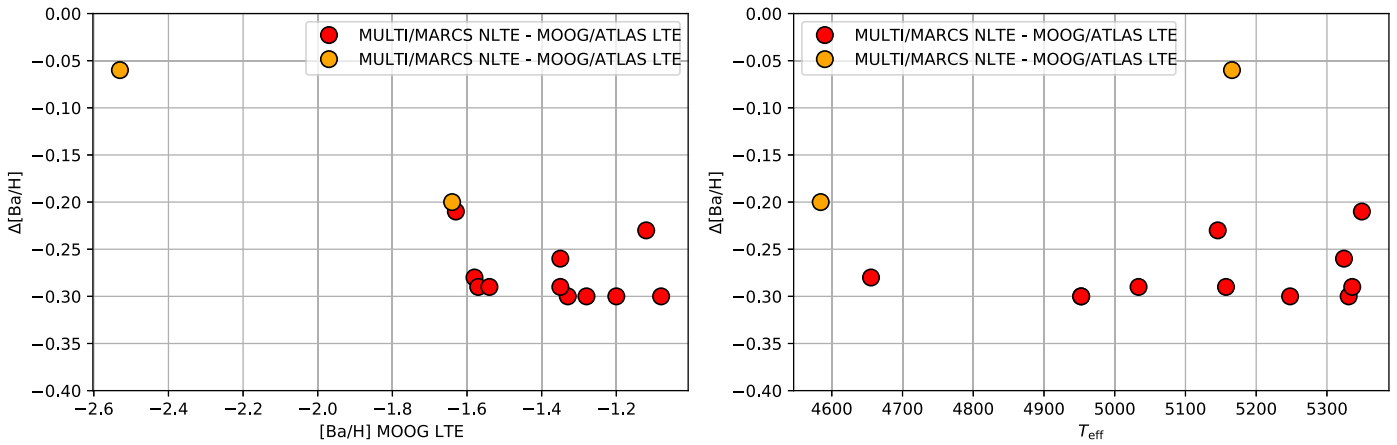
Figure 11. Differences between NLTE (MULTI/MARCS) and LTE (MOOG/ATLAS) abundances for stars with S/N > 25. Left: differences as a function of [Ba/H] (LTE). Right: differences as a function of $T_{\rm eff}$. The NLTE correction for saturated lines clusters closely around Δ[Ba/H] = -0.27 ± 0.04 (the outlier is the candidate member Star 14 with a relatively low [Ba/H] abundance).
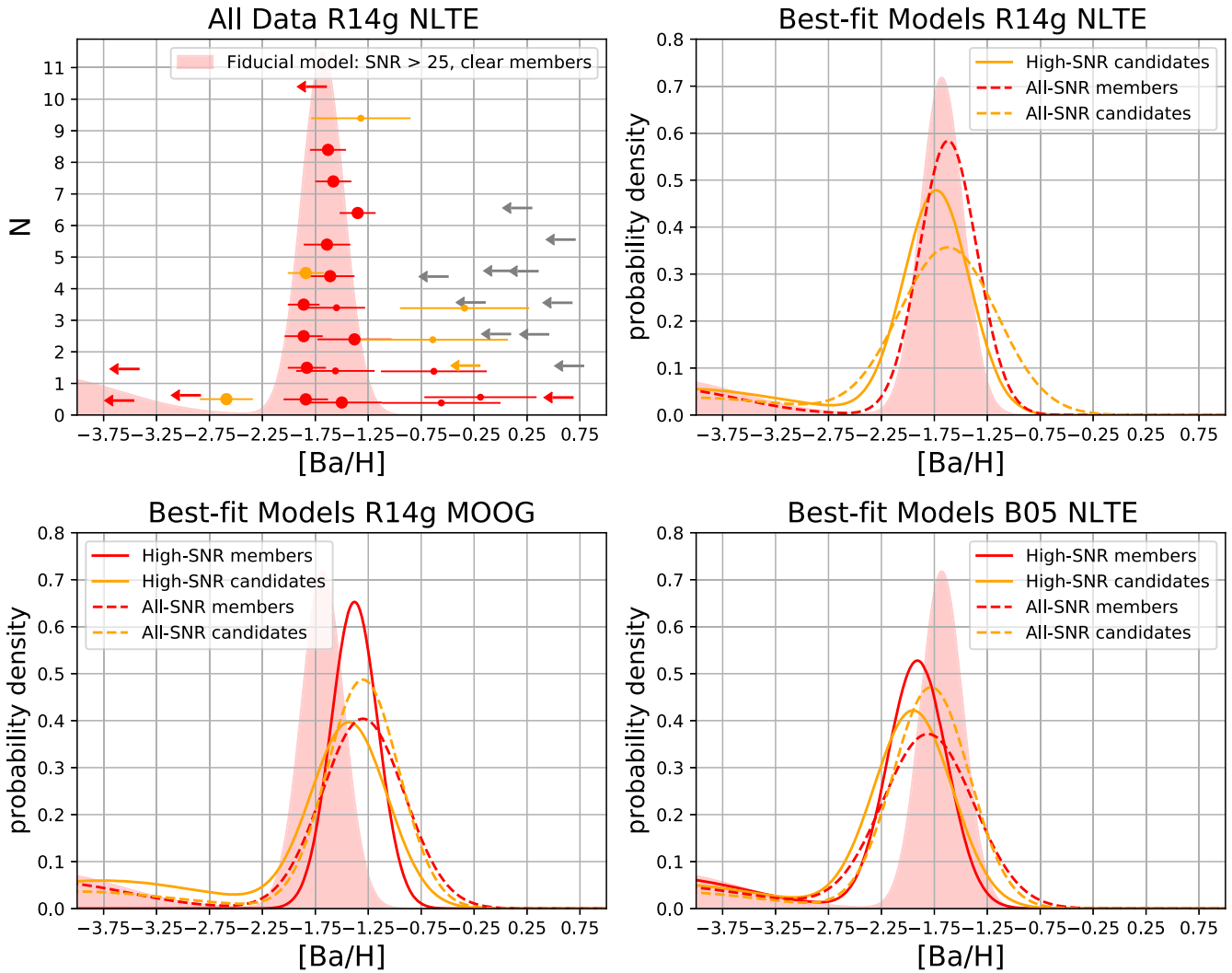

Figure 12. Exploration of different best-fit models by permuting the data sample (top-right panel), radiative transfer (bottom-left panel), and $\log g$–ν_t relation (bottom-right panel).

several permutations of best-fit [Ba/H] distributions in Figure 12. The top-left panel shows the R14g and NLTE abundances used in the main paper, but plotting all low-S/N

detections as small data points and low-S/N upper limits as gray arrows. As also seen in the right column of Figure 9, the low-S/N data are skewed toward higher [Ba/H] abundances primarily due

Table 9
[Ba/H] Distribution Fits (Stars with S/N > 25)

Data	μ_1	σ_1	σ_1 limit	μ_2	σ_2	p_2
R14g MULTI NLTE members	$-1.68^{+0.07}_{-0.07}$	$0.05^{+0.08}_{-0.03}$	<0.20	$-4.32^{+0.49}_{-0.46}$	$0.08^{+0.32}_{-0.06}$	$0.28^{+0.12}_{-0.10}$
R14g MOOG LTE members	$-1.38^{+0.06}_{-0.06}$	$0.06^{+0.09}_{-0.05}$	<0.22	$-4.26^{+0.53}_{-0.50}$	$0.09^{+0.32}_{-0.07}$	$0.28^{+0.12}_{-0.10}$
B05 MULTI NLTE members	$-1.91^{+0.07}_{-0.06}$	$0.11^{+0.10}_{-0.08}$	<0.28	$-4.31^{+0.49}_{-0.47}$	$0.09^{+0.36}_{-0.07}$	$0.26^{+0.12}_{-0.10}$
B05 MOOG LTE members	$-1.60^{+0.07}_{-0.07}$	$0.14^{+0.09}_{-0.09}$	<0.30	$-4.22^{+0.48}_{-0.51}$	$0.11^{+0.37}_{-0.09}$	$0.23^{+0.14}_{-0.13}$
R14g MULTI NLTE with candidates	$-1.73^{+0.07}_{-0.08}$	$0.12^{+0.11}_{-0.09}$	<0.31	$-4.12^{+0.57}_{-0.56}$	$0.23^{+0.55}_{-0.20}$	$0.26^{+0.12}_{-0.11}$
R14g MOOG LTE with candidates	$-1.43^{+0.07}_{-0.08}$	$0.13^{+0.13}_{-0.09}$	<0.36	$-3.77^{+0.62}_{-0.69}$	$0.62^{+0.28}_{-0.50}$	$0.29^{+0.14}_{-0.11}$
B05 MULTI NLTE with candidates	$-1.95^{+0.07}_{-0.04}$	$0.19^{+0.10}_{-0.10}$	<0.37	$-4.25^{+0.52}_{-0.51}$	$0.10^{+0.46}_{-0.08}$	$0.22^{+0.12}_{-0.09}$
B05 MOOG LTE with candidates	$-1.69^{+0.11}_{-0.10}$	$0.24^{+0.11}_{-0.10}$	<0.46	$-3.83^{+0.74}_{-0.61}$	$0.40^{+0.44}_{-0.37}$	$0.25^{+0.15}_{-0.13}$

to bad sky subtraction (Figure 3). The top-right panel shows three alternate fits to different permutations of data used (members and candidates; high- and low-S/N data). The bottom-left panel shows the effect of changing the radiative transfer, and the bottom-right panel shows the effect of changing the microturbulence relation. These differences make a relatively small change to the Ba dispersion (which is not resolved) but a fairly large change to the mean abundance.

Appendix D
Additional Chemical Abundances

Table 10 shows member stars with sufficiently high S/N in the M2FS HiRes Mg b data to measure detailed chemical abundances. This illustrates the usefulness of the M2FS Mg Wide configuration for measuring detailed chemical abundances in metal-poor stars.

Table 10
M2FS Mg b Abundances

ID	S/N	[Mg/H]	σ_{Mg}	[Ca/H]	σ_{Ca}	[Ti/H]	σ_{Ti}	[Cr/H]	σ_{Cr}	[Fe/H]	σ_{Fe}	[Nd/H]	σ_{Nd}
2	39.3	−2.48	0.12	−2.21	0.07	−2.29	0.10	−2.83	0.13	−2.63	0.11	−1.20	0.09
3	34.2	−2.59	0.13	−2.38	0.07	−2.57	0.08	−3.35	0.11	−2.78	0.13	−1.35	0.08
4	37.3	−2.55	0.11	−2.47	0.08	−2.71	0.08	−3.38	0.09	−3.14	0.08	⋯	⋯
5	19.4	−2.52	0.13	−1.86	0.13	−1.65	0.19	−2.10	0.20	−1.93	0.17	−0.89	0.15
6	23.5	−2.75	0.13	−2.24	0.15	−2.55	0.10	⋯	⋯	−2.81	0.12	⋯	⋯
7	13.8	−2.67	0.22	⋯	⋯	⋯	⋯	⋯	⋯	⋯	⋯	⋯	⋯
8	15.2	−2.03	0.16	−1.52	0.17	−1.76	0.14	−2.42	0.23	−2.17	0.12	−0.90	0.12
9	17.0	−2.72	0.13	⋯	⋯	−2.55	0.12	−3.32	0.14	−2.67	0.11	⋯	⋯
10	15.3	−2.09	0.18	⋯	⋯	−2.44	0.17	−3.49	0.16	−2.86	0.16	⋯	⋯
12	15.2	−2.84	0.15	−1.94	0.16	−2.40	0.13	−3.07	0.22	⋯	⋯	⋯	⋯
13	9.9	−2.60	0.16	⋯	⋯	⋯	⋯	−2.46	0.27	⋯	⋯	⋯	⋯

ORCID iDs

Alexander P. Ji ![orcid] https://orcid.org/0000-0002-4863-8842
Joshua D. Simon ![orcid] https://orcid.org/0000-0002-4733-4994
Ian U. Roederer ![orcid] https://orcid.org/0000-0001-5107-8930
Ekaterina Magg ![orcid] https://orcid.org/0000-0001-8784-6794
Anna Frebel ![orcid] https://orcid.org/0000-0002-2139-7145
Christian I. Johnson ![orcid] https://orcid.org/0000-0002-8878-3315
Ralf S. Klessen ![orcid] https://orcid.org/0000-0002-0560-3172
Mattis Magg ![orcid] https://orcid.org/0000-0002-9022-5136
Gabriele Cescutti ![orcid] https://orcid.org/0000-0002-3184-9918
Mario Mateo ![orcid] https://orcid.org/0000-0002-3856-232X
Maria Bergemann ![orcid] https://orcid.org/0000-0002-9908-5571
John I. Bailey, III ![orcid] https://orcid.org/0000-0002-4272-263X

References

Abohalima, A., & Frebel, A. 2018, ApJS, 238, 36
Applebaum, E., Brooks, A. M., Christensen, C. R., et al. 2021, ApJ, 906, 96
Asplund, M., Grevesse, N., Sauval, A. J., & Scott, P. 2009, ARA&A, 47, 481
Aubert, D., Deparis, N., Ocvirk, P., et al. 2018, ApJL, 856, L22
Barklem, P. S., Christlieb, N., Beers, T. C., et al. 2005, A&A, 439, 129
Barklem, P. S., Piskunov, N., & O'Mara, B. J. 2000, A&AS, 142, 467
Battaglia, G., Irwin, M., Tolstoy, E., et al. 2008, MNRAS, 383, 183
Battaglia, G., Taibi, S., Thomas, G. F., & Fritz, T. K. 2022, A&A, 657, A54
Bechtol, K., Drlica-Wagner, A., Balbinot, E., et al. 2015, ApJ, 807, 50
Beniamini, P., Dvorkin, I., & Silk, J. 2018, MNRAS, 478, 1994
Beniamini, P., & Hotokezaka, K. 2020, MNRAS, 496, 1891
Beniamini, P., Hotokezaka, K., & Piran, T. 2016, ApJL, 829, L13
Beniamini, P., & Piran, T. 2019, MNRAS, 487, 4847
Benson, A. J., Frenk, C. S., Lacey, C. G., Baugh, C. M., & Cole, S. 2002, MNRAS, 333, 177
Bergemann, M., Collet, R., Amarsi, A. M., et al. 2017, ApJ, 847, 15
Bergemann, M., Gallagher, A. J., Eitner, P., et al. 2019, A&A, 631, A80
Bergemann, M., Lind, K., Collet, R., Magic, Z., & Asplund, M. 2012, MNRAS, 427, 27
Bergemann, M., & Nordlander, T. 2014, arXiv:1403.3088
Bernstein, R., Shectman, S. A., Gunnels, S. M., Mochnacki, S., & Athey, A. E. 2003, Proc. SPIE, 4841, 1694
Bertin, E., & Arnouts, S. 1996, A&AS, 117, 393
Binney, J., & Tremaine, S. 2008, Galactic Dynamics: Second Edition (Princeton, NJ: Princeton Univ. Press)
Blackwell, D. E., Petford, A. D., Shallis, M. J., & Simmons, G. J. 1982, MNRAS, 199, 43
Bland-Hawthorn, J., Sutherland, R., & Webster, D. 2015, ApJ, 807, 154
Bonetti, M., Perego, A., Dotti, M., & Cescutti, G. 2019, MNRAS, 490, 296
Bose, S., Deason, A. J., & Frenk, C. S. 2018, ApJ, 863, 123
Bovill, M. S., & Ricotti, M. 2009, ApJ, 693, 1859
Brauer, K., Ji, A. P., Drout, M. R., & Frebel, A. 2021, ApJ, 915, 81
Brauer, K., Ji, A. P., Frebel, A., et al. 2019, ApJ, 871, 247
Brown, T. M., Tumlinson, J., Geha, M., et al. 2014, ApJ, 796, 91
Bullock, J. S., Kravtsov, A. V., & Weinberg, D. H. 2000, ApJ, 539, 517
Carlsson, M. 1986, UppOR, 33, 39
Carpenter, B., Gelman, A., Hoffman, M., et al. 2017, J. Stat. Softw., 76, 1
Casagrande, L., & VandenBerg, D. A. 2014, MNRAS, 444, 392
Casey, A. R. 2014, arXiv:1405.5968
Casey, A. R., Ji, A. P., Hansen, T. T., et al. 2021, ApJ, 921, 67
Castelli, F., & Kurucz, R. L. 2003, in IAU Symp. 210, Modelling of Stellar Atmospheres, ed. N. Piskunov, W. W. Weiss, & D. F. Gray (San Francisco, CA: ASP)
Cavallo, L., Cescutti, G., & Matteucci, F. 2021, MNRAS, 503, 1
Chiaki, G., Susa, H., & Hirano, S. 2018, MNRAS, 475, 4378
Chiti, A., Frebel, A., Ji, A. P., et al. 2022, arXiv:2205.01740
Chiti, A., Frebel, A., Simon, J. D., et al. 2021, NatAs, 5, 392
Chornock, R., Berger, E., Kasen, D., et al. 2017, ApJL, 848, L19
Cioffi, D. F., McKee, C. F., & Bertschinger, E. 1988, ApJ, 334, 252
Cohen, J. G., Christlieb, N., Thompson, I., et al. 2013, ApJ, 778, 56
Côté, B., Fryer, C. L., Belczynski, K., et al. 2018, ApJ, 855, 99
Cowan, J. J., Sneden, C., Lawler, J. E., et al. 2021, RvMP, 93, 015002
de Avillez, M. A., & Mac Low, M.-M. 2002, ApJ, 581, 1047
Dekel, A., & Woo, J. 2003, MNRAS, 344, 1131
DES Collaboration, Abbott, T. M. C., Abdalla, F. B., et al. 2018, ApJS, 239, 18

Dotter, A., Chaboyer, B., Jevremović, D., et al. 2008, ApJS, 178, 89
Drout, M. R., Piro, A. L., Shappee, B. J., et al. 2017, Sci, 358, 1570
Emerick, A., Bryan, G. L., Mac Low, M.-M., et al. 2018, ApJ, 869, 94
Emerick, A., Bryan, G. L., & Mac Low, M.-M. 2019, MNRAS, 482, 1304
Emerick, A., Bryan, G. L., & Mac Low, M.-M. 2020, ApJ, 890, 155
Erkal, D., & Belokurov, V. A. 2020, MNRAS, 495, 2554
Escala, I., Wetzel, A., Kirby, E. N., et al. 2018, MNRAS, 474, 2194
Foreman-Mackey, D., Hogg, D. W., Lang, D., & Goodman, J. 2013, PASP, 125, 306
Frebel, A., & Bromm, V. 2012, ApJ, 759, 115
Frebel, A., Casey, A. R., Jacobson, H. R., & Yu, Q. 2013, ApJ, 769, 57
Frebel, A., & Norris, J. E. 2015, ARA&A, 53, 631
Frebel, A., Norris, J. E., Gilmore, G., & Wyse, R. F. G. 2016, ApJ, 826, 110
Frebel, A., Simon, J. D., Geha, M., & Willman, B. 2010, ApJ, 708, 560
Frebel, A., Simon, J. D., & Kirby, E. N. 2014, ApJ, 786, 74
Frischknecht, U., Hirschi, R., Pignatari, M., et al. 2016, MNRAS, 456, 1803
Fryer, C. L., Herwig, F., Hungerford, A., & Timmes, F. X. 2006, ApJL, 646, L131
Gaia Collaboration, Brown, A. G. A., Vallenari, A., et al. 2021, A&A, 649, A1
Gaia Collaboration, Prusti, T., de Bruijne, J. H. J., et al. 2016, A&A, 595, A1
Gallagher, A. J., Bergemann, M., Collet, R., et al. 2020, A&A, 634, A55
Grand, R. J. J., Gómez, F. A., Marinacci, F., et al. 2017, MNRAS, 467, 179
Gray, D. F. 2008, The Observation and Analysis of Stellar Photospheres
Greif, T. H., Glover, S. C. O., Bromm, V., & Klessen, R. S. 2010, ApJ, 716, 510
Greif, T. H., Johnson, J. L., Bromm, V., & Klessen, R. S. 2007, ApJ, 670, 1
Greif, T. H., Johnson, J. L., Klessen, R. S., & Bromm, V. 2008, MNRAS, 387, 1021
Grichener, A., Kobayashi, C., & Soker, N. 2022, ApJL, 926, L9
Grichener, A., & Soker, N. 2019, arXiv:1909.06328
Gustafsson, B., Edvardsson, B., Eriksson, K., et al. 2008, A&A, 486, 951
Hansen, T. T., Andersen, J., Nordström, B., et al. 2015, A&A, 583, A49
Hansen, T. T., Andersen, J., Nordström, B., et al. 2016, A&A, 588, A3
Hansen, T. T., Marshall, J. L., Simon, J. D., et al. 2020, ApJ, 897, 183
Hansen, T. T., Simon, J. D., Marshall, J. L., et al. 2017, ApJ, 838, 44
Hasselquist, S., Shetrone, M., Smith, V., et al. 2017, ApJ, 845, 162
Hill, V., Skúladóttir, Á., Tolstoy, E., et al. 2019, A&A, 626, A15
Hirai, Y., Ishimaru, Y., Saitoh, T. R., et al. 2015, ApJ, 814, 41
Hirai, Y., Ishimaru, Y., Saitoh, T. R., et al. 2017, MNRAS, 466, 2474
Hunter, J. D. 2007, CSE, 9, 90
Ivans, I. I., Simmerer, J., Sneden, C., et al. 2006, ApJ, 645, 613
Jacobson, H. R., Keller, S., Frebel, A., et al. 2015, ApJ, 807, 171
Jeon, M., Besla, G., & Bromm, V. 2017, ApJ, 848, 85
Jeon, M., Besla, G., & Bromm, V. 2021, MNRAS, 506, 1850
Jeon, M., Pawlik, A. H., Bromm, V., & Milosavljević, M. 2014, MNRAS, 444, 3288
Ji, A., Beaton, R., Chakrabarti, S., et al. 2019a, BAAS, 51, 166
Ji, A. P., Drout, M. R., & Hansen, T. T. 2019b, ApJ, 882, 40
Ji, A. P., & Frebel, A. 2018, ApJ, 856, 138
Ji, A. P., Frebel, A., & Bromm, V. 2015, MNRAS, 454, 659
Ji, A. P., Frebel, A., Chiti, A., & Simon, J. D. 2016a, Natur, 531, 610
Ji, A. P., Frebel, A., Simon, J. D., & Chiti, A. 2016b, ApJ, 830, 93
Ji, A. P., Frebel, A., Simon, J. D., & Geha, M. 2016c, ApJ, 817, 41
Ji, A. P., Li, T. S., Hansen, T. T., et al. 2020a, AJ, 160, 181
Ji, A. P., Li, T. S., Simon, J. D., et al. 2020b, ApJ, 889, 27
Ji, A. P., Simon, J. D., Frebel, A., Venn, K. A., & Hansen, T. T. 2019c, ApJ, 870, 83
Jones, E., Oliphant, T., Peterson, P., et al. 2001, SciPy: Open Source Scientific Tools for Python (Austin, TX: SciPy), http://www.scipy.org/
Karlsson, T. 2005, A&A, 439, 93
Karlsson, T., Johnson, J. L., & Bromm, V. 2008, ApJ, 679, 6
Kelson, D. D. 2003, PASP, 115, 688
Kilpatrick, C. D., Foley, R. J., Kasen, D., et al. 2017, Sci, 358, 1583
Kirby, E. N., Gilbert, K. M., Escala, I., et al. 2020, AJ, 159, 46
Kirby, E. N., Martin, C. L., & Finlator, K. 2011, ApJL, 742, L25
Klessen, R. S., & Hennebelle, P. 2010, A&A, 520, A17
Klessen, R. S., & Lin, D. N. 2003, PhRvE, 67, 046311
Kobulnicky, H. A., & Skillman, E. D. 1997, ApJ, 489, 636
Koch, A., Feltzing, S., Adén, D., & Matteucci, F. 2013, A&A, 554, A5
Koch, A., McWilliam, A., Grebel, E. K., Zucker, D. B., & Belokurov, V. 2008, ApJL, 688, L13
Komiya, Y., & Shigeyama, T. 2016, ApJ, 830, 76
Koposov, S. E., Belokurov, V., Torrealba, G., & Evans, N. W. 2015a, ApJ, 805, 130
Koposov, S. E., Casey, A. R., Belokurov, V., et al. 2015b, ApJ, 811, 62
Koposov, S. E., Walker, M. G., Belokurov, V., et al. 2018, MNRAS, 479, 5343

Kramida, A., Ralchenko, Y., Reader, J. & NIST ASD Team 2019, NIST Atomic Spectra Database (version 5.7.1) (Gaithersburg, MD: National Institute of Standards and Technology)

Krumholz, M. R., & Ting, Y.-S. 2018, MNRAS, 475, 2236

Kurucz, R., & Bell, B. 1995, in Atomic Line Data, Kurucz CD-ROM No. 23., ed. R. Kurucz & B. Bell (Cambridge, MA: Smithsonian Astrophysical Observatory), 23, Atomic Line Data, CD-ROM No..Kurucz23

Lacchin, E., Matteucci, F., Vincenzo, F., & Palla, M. 2020, MNRAS, 495, 3276

Li, T. S., Koposov, S. E., Zucker, D. B., et al. 2019, MNRAS, 490, 3508

Li, T. S., Simon, J. D., Pace, A. B., et al. 2018, ApJ, 857, 145

Limongi, M., & Chieffi, A. 2018, ApJS, 237, 13

Lindegren, L., Klioner, S. A., Hernández, J., et al. 2021, A&A, 649, A2

Lunnan, R., Vogelsberger, M., Frebel, A., et al. 2012, ApJ, 746, 109

Macias, P., & Ramirez-Ruiz, E. 2019, ApJL, 877, L24

Magain, P. 1984, A&A, 134, 189

Magg, M., Nordlander, T., Glover, S. C. O., et al. 2020, MNRAS, 498, 3703

Magg, M., Schauer, A. T. P., Klessen, R. S., et al. 2022, ApJ, 929, 119

Marino, A. F., Villanova, S., Piotto, G., et al. 2008, A&A, 490, 625

Marshall, J. L., Hansen, T., Simon, J. D., et al. 2018, arXiv:1812.01022

Martini, P., Kelson, D. D., Kim, E., Mulchaey, J. S., & Athey, A. A. 2006, ApJ, 644, 116

Mashonkina, L., Christlieb, N., & Eriksson, K. 2014, A&A, 569, A43

Mashonkina, L., Korn, A. J., & Przybilla, N. 2007, A&A, 461, 261

Mashonkina, L., Sitnova, T., & Belyaev, A. K. 2017, A&A, 605, A53

Mashonkina, L. I., Sitnova, T. N., & Pakhomov, Y. V. 2016, AstL, 42, 606

Mateo, M., Bailey, J. I., Crane, J., et al. 2012, Proc. SPIE, 8446, 84464Y

McConnachie, A. W., & Venn, K. A. 2020, RNAAS, 4, 229

McKinney, W. 2010, in Proc. of the 9th Python in Science Conf. (Austin, TX: SciPy), 56

McQuinn, K. B. W., Skillman, E. D., Dolphin, A., et al. 2015, ApJL, 815, L17

McWilliam, A., Wallerstein, G., & Mottini, M. 2013, ApJ, 778, 149

Miller, J. M., Sprouse, T. M., Fryer, C. L., et al. 2020, ApJ, 902, 66

Minor, Q. E., Pace, A. B., Marshall, J. L., & Strigari, L. E. 2019, MNRAS, 487, 2961

Molero, M., Romano, D., Reichert, M., et al. 2021, MNRAS, 505, 2913

Mösta, P., Roberts, L. F., Halevi, G., et al. 2018, ApJ, 864, 171

Muñoz, R. R., Côté, P., Santana, F. A., et al. 2018, ApJ, 860, 66

Mutlu-Pakdil, B., Sand, D. J., Carlin, J. L., et al. 2018, ApJ, 863, 25

O'Brian, T. R., Wickliffe, M. E., Lawler, J. E., Whaling, W., & Brault, J. W. 1991, JOSAB, 8, 1185

Ojima, T., Ishimaru, Y., Wanajo, S., Prantzos, N., & François, P. 2018, ApJ, 865, 87

Okamoto, T., Gao, L., & Theuns, T. 2008, MNRAS, 390, 920

Pan, L., Scannapieco, E., & Scalo, J. 2013, ApJ, 775, 111

Pasquini, L., Avila, G., Blecha, A., et al. 2002, Msngr, 110, 1

Patel, E., Kallivayalil, N., Garavito-Camargo, N., et al. 2020, ApJ, 893, 121

Placco, V. M., Sneden, C., Roederer, I. U., et al. 2021, RNAAS, 5, 92

Price-Whelan, A. M., Sipőcz, B. M., Günther, H. M., et al. 2018, AJ, 156, 123

Radice, D., Perego, A., Hotokezaka, K., et al. 2018, ApJ, 869, 130

Revaz, Y., Arnaudon, A., Nichols, M., Bonvin, V., & Jablonka, P. 2016, A&A, 588, A21

Ritter, J. S., Sluder, A., Safranek-Shrader, C., Milosavljević, M., & Bromm, V. 2015, MNRAS, 451, 1190

Robertson, B., Bullock, J. S., Font, A. S., Johnston, K. V., & Hernquist, L. 2005, ApJ, 632, 872

Robin, A. C., Reylé, C., Derrière, S., & Picaud, S. 2003, A&A, 409, 523

Astropy Collaboration, Robitaille, T. P., Tollerud, E. J., et al. 2013, A&A, 558, A33

Rodriguez Wimberly, M. K., Cooper, M. C., Fillingham, S. P., et al. 2019, MNRAS, 483, 4031

Roederer, I. U. 2017, ApJ, 835, 23

Roederer, I. U., Mateo, M., Bailey, J. I., et al. 2016a, MNRAS, 455, 2417

Roederer, I. U., Mateo, M., Bailey, J. I., III, et al. 2016b, AJ, 151, 82

Roederer, I. U., Preston, G. W., Thompson, I. B., et al. 2014, AJ, 147, 136

Ryabchikova, T., Piskunov, N., Kurucz, R. L., et al. 2015, PhyS, 90, 054005

Ryan, S. G., Norris, J. E., & Beers, T. C. 1996, ApJ, 471, 254

Sacchi, E., Richstein, H., Kallivayalil, N., et al. 2021, ApJL, 920, L19

Safarzadeh, M., Ramirez-Ruiz, E., Andrews, J. J., et al. 2019a, ApJ, 872, 105

Safarzadeh, M., Sarmento, R., & Scannapieco, E. 2019b, ApJ, 876, 28

Safarzadeh, M., & Scannapieco, E. 2017, MNRAS, 471, 2088

Safranek-Shrader, C., Agarwal, M., Federrath, C., et al. 2012, MNRAS, 426, 1159

Salvadori, S., & Ferrara, A. 2009, MNRAS, 395, L6

Santana, F. A., Muñoz, R. R., Geha, M., et al. 2013, ApJ, 774, 106

Schönrich, R. A., & Weinberg, D. H. 2019, MNRAS, 487, 580

Siegel, D. M., Barnes, J., & Metzger, B. D. 2019, Natur, 569, 241

Simon, J. D. 2019, ARA&A, 57, 375

Simon, J. D., Brown, T. M., Mutlu-Pakdil, B., et al. 2022, ApJ, arXiv:2212.00810

Simon, J. D., Drlica-Wagner, A., Li, T. S., et al. 2015, ApJ, 808, 95

Simon, J. D., Frebel, A., McWilliam, A., Kirby, E. N., & Thompson, I. B. 2010, ApJ, 716, 446

Simon, J. D., Li, T. S., Drlica-Wagner, A., et al. 2017, ApJ, 838, 11

Simon, J. D., Li, T. S., Erkal, D., et al. 2020, ApJ, 892, 137

Smith, G., & Raggett, D. S. J. 1981, JPhB, 14, 4015

Sneden, C., Cowan, J. J., & Gallino, R. 2008, ARA&A, 46, 241

Sneden, C. A. 1973, PhD thesis, The Univ. Texas at Austin

Sobeck, J. S., Kraft, R. P., Sneden, C., et al. 2011, AJ, 141, 175

Speagle, J. S. 2020, MNRAS, 493, 3132

Surman, R., McLaughlin, G. C., & Hix, W. R. 2006, ApJ, 643, 1057

Tanaka, M., Utsumi, Y., Mazzali, P. A., et al. 2017, PASJ, 69, 102

Tanvir, N. R., Levan, A. J., González-Fernández, C., et al. 2017, ApJL, 848, L27

Tarumi, Y., Suda, T., van de Voort, F., et al. 2021, MNRAS, 505, 3755

Tarumi, Y., Yoshida, N., & Inoue, S. 2020, MNRAS, 494, 120

Theler, R., Jablonka, P., Lucchesi, R., et al. 2020, A&A, 642, A176

Tody, D. 1986, Proc. SPIE, 627, 733

Tody, D. 1993, in ASP Conf. Ser. 52, Astronomical Data Analysis Software and Systems II, ed. R. J. Hanisch, R. J. V. Brissenden, & J. Barnes (San Francisco, CA: ASP), 173

Tolstoy, E., Hill, V., & Tosi, M. 2009, ARA&A, 47, 371

Tsujimoto, T., Matsuno, T., Aoki, W., Ishigaki, M. N., & Shigeyama, T. 2017, ApJL, 850, L12

van der Walt, S., Colbert, S. C., & Varoquaux, G. 2011, CSE, 13, 22

Vargas, L. C., Geha, M., Kirby, E. N., & Simon, J. D. 2013, ApJ, 767, 134

Venn, K. A., Irwin, M., Shetrone, M. D., et al. 2004, AJ, 128, 1177

Venn, K. A., Starkenburg, E., Malo, L., Martin, N., & Laevens, B. P. M. 2017, MNRAS, 466, 3741

Walker, M. G., Mateo, M., Olszewski, E. W., et al. 2015, ApJ, 808, 108

Waskom, M., Botvinnik, O., O'Kane, D., et al. 2016, seaborn: v0.7.0 (January 2016), Zenodo, doi:10.5281/zenodo.45133

Webster, D., Bland-Hawthorn, J., & Sutherland, R. 2015, ApJL, 799, L21

Webster, D., Frebel, A., & Bland-Hawthorn, J. 2016, ApJ, 818, 80

Webster, D., Sutherland, R., & Bland-Hawthorn, J. 2014, ApJ, 796, 11

Weidner, C., Kroupa, P., Pflamm-Altenburg, J., & Vazdekis, A. 2013, MNRAS, 436, 3309

Weisz, D. R., Dolphin, A. E., Skillman, E. D., et al. 2014a, ApJ, 789, 147

Weisz, D. R., Dolphin, A. E., Skillman, E. D., et al. 2014b, ApJ, 789, 148

Wenger, M., Ochsenbein, F., Egret, D., et al. 2000, A&AS, 143, 9

Wheeler, C., Hopkins, P. F., Pace, A. B., et al. 2019, MNRAS, 490, 4447

Willman, B., & Strader, J. 2012, AJ, 144, 76

Wise, J. H., & Abel, T. 2007, ApJ, 665, 899

Wolf, J., Martinez, G. D., Bullock, J. S., et al. 2010, MNRAS, 406, 1220

Wu, M.-R., Fernández, R., Martínez-Pinedo, G., & Metzger, B. D. 2016, MNRAS, 463, 2323

Zechmeister, M., Anglada-Escudé, G., & Reiners, A. 2014, A&A, 561, A59